

Imaging on Underwater Moving Targets with Multistatic Synthetic Aperture Sonar

Chou-Wei Kiang and Jean-Fu Kiang

Abstract—A multistatic synthetic aperture sonar (SAS) configuration, composed of an active sonar, a towed receiver and a sonobuoy, is proposed to acquire the image of a moving target and estimate its velocity vector. The range model incorporates the time delay of an acoustic pulse between its emission and backscattered from the target to the receivers. An image is acquired from the received signals at one receiver after range cell migration correction (RCMC), range walk compensation (RWC) and compression, without prior knowledge on the motion parameters of the target. Range-frequency reversal transform (RFRT) and a modified second-order Wigner-Ville distribution (SoWVD) are used to estimate the chirp rate in the range model, and Radon transform is used to estimate the Doppler centroid. The velocity vector of the moving target is accurately estimated, within 3% of error and insensitive to noise, by using the Doppler centroids derived from the signals at the three receivers. Eight different scenarios are simulated to demonstrate the efficacy of the proposed method. The shape and size of the moving target can be clearly identified in all but one case. Three state-of-the-art methods are also used to verify the accuracy of the proposed method, the effects of noise are analyzed, and autofocus algorithms are applied to enhance the acquired images in some difficult cases.

Index Terms—Synthetic aperture sonar (SAS), multistatic, moving target, velocity vector, range cell migration correction (RCMC), range walk compensation (RWC), range-frequency reversal transform (RFRT), second-order Wigner-Ville distribution (SoWVD), Radon transform.

I. INTRODUCTION

Tremendous progress has been made over decades in technologies for tracking submarines and underwater moving vehicles (UAVs), which can be categorized into acoustic and non-acoustic types [1]. The non-acoustic type includes the detection of magnetic anomaly, heat, optical reflection and seawater displacement [2]. A submarine can be detected a few kilometers away by sensing the magnetic field disturbed by its ferromagnetic shell [2], [3]. Light detection and ranging (LiDAR) emitting blue and green light pulses can be used to detect a submarine by observing possible reflection or absorption of pulses by its hull [1], [2].

Various sonar systems [1], [4] have been developed for underwater environment monitoring, military surveillance, underwater vehicle detection [5], [6], and so on. An active scanning sonar can simultaneously search for submarines in many different directions and ranges by sending pings and listening to their echoes [7]. An active dipping sonar, tethered to a helicopter [8], [9], can be deployed at a given depth to detect

C.-W. Kiang and J.-F. Kiang are with the Department of Electrical Engineering, National Taiwan University, Taipei, Taiwan 10617. E-mail: jfkiang@ntu.edu.tw.

submarine movements. An active sonar has the drawback of exposing its position when sending sound bursts [1], [2]. On the other hand, a passive sonar, which is usually composed of an array of underwater hydrophones, can eavesdrop the sound features generated by moving UAVs without being noticed [1], [2]. On the other hand, advancement of stealth technologies has imposed more challenges on conventional passive sonars [2], [10].

Conventional sonars were designed to detect the direction and range of a target, but not its size or shape [10]. Synthetic aperture sonar (SAS) operates by periodically sending acoustic bursts from an active sidescan sonar on a moving platform and using their echoes from a target over a finite time window to acquire the target image [11]. Since the 1990s, SAS experiments have been carried out with sonar installed on an underwater cable-towed platform to reduce the motion perturbation and noise of the host ship [11], [12]. SAS has been used for submarine prospecting and bathymetry [11], [13], identifying stationary targets [14], [15], [16], and so on.

There are far fewer articles on SAS imaging than on synthetic aperture radar (SAR), its air counterpart. The major differences between them are the signal speed and their application environments. Some state-of-the-art (SOTA) algorithms for SAR can be extended for SAS imaging after significant modifications to make up the stop-and-go approximation [13] generally adopted for SAR imaging. Other commonly used SAR imaging techniques on ground moving target (GMT) [17], [18], including range cell migration correction (RCMC) and range walk compensation (RWC) [19], can also be adapted for SAS imaging, with the prior knowledge of motion parameters of a moving target [20], [21], or without them as in [19], conducted with Keystone transform and matched filter.

In [22], a focusing algorithm on fast moving targets was proposed. Hough transform was applied to compensate the range walk effect, followed by a polynomial Fourier transform (PFT) to estimate the second-order and third-order Doppler parameters of the GMT, rendering the motion parameters as byproducts. In [23], a polynomial Radon transform (PRT) was applied to compensate for the range walk and range cell migration of a high-speed moving target, followed by a PFT to compensate for the Doppler migration.

Radon transform was claimed to estimate more accurate slope of signal traces than Hough transform [24]. In [25], [26], an image of a moving target was focused without knowing its velocity. Then, Hough or Radon transform was applied to estimate the slope of signal traces in a time-frequency plane, followed by solving a 2D optimization problem to estimate the azimuth frequency modulation (FM) rate and Doppler centroid

frequency, which were related to range cell migration and range walk, respectively [19], [27].

In [28], a joint time-frequency analysis (JTFA) was proposed for SAS imaging, in a sequence of short-time Fourier transform (STFT), Wigner-Ville distribution (WVD), Cohens class, time-frequency distribution series, and adaptive chirplet transform. The range model was based on the stop-and-go assumption, and the target was modeled as 14 point scatterers.

In [29], a Radon transform-cubic chirplet decomposition (RTCCD) method was proposed for ISAS imaging of underwater vehicles with simple rotational motion, with one sonar sending amplitude modulated-cubic phase signal (AM-CPS). The underwater vehicle was modeled as a bunch of about 100 point targets, immersed in a simple unperturbed environment.

In [30], [31], SAS imaging was conducted on seafloor (seabed). In [13], [32], [33], SAS imaging was conducted on received signals from simulated point targets and real seafloor, respectively. The spatial resolution required for seafloor imaging was not fine enough to acquire image of moving target.

In [34], the signature of moving targets in SAS seafloor imaging was qualitatively analyzed. In [35], [36], SAS methods were proposed for detecting targets buried or lying on the seabed, and a deep convolutional neural network method was proposed to classify stationary targets in SAS images [37].

In [38], it was mentioned that residual aperture errors due to imperfect motion compensation would blur the image, which could be remedied with autofocusing methods such as phase gradient autofocus (PGA). It was also mentioned that low acoustic speed constrained the sampling rate, causing aliasing effects, and higher-order phase error should be considered when the relative velocity between sonar and target is large. The SOTA algorithms of strip-map SAS were summarized, including a brute-force exact image reconstruction algorithm, an exact transfer function algorithm for focusing image, range-Doppler algorithm (RDA), chirp scaling algorithm (CSA) [11], and wavenumber algorithm [39].

In [13], CSA was proposed to acquire SAS images of seafloor. Compared with RDA, the RCMC was done in a 2D frequency domain with a phase multiplier, which was more accurate but time consuming. In [32], an omega-K algorithm was applied for SAS imaging of seafloor. In [33], an algorithm for multistatic SAS imaging on seafloor was proposed, considering the time delay between signal emission and reception. A point target reference spectrum (PTRS), azimuth modulation, and coupling terms were derived to constitute a fast imaging algorithm. A wavenumber-based algorithm was used to decouple bulk and differential RCMs embedded in the received signals. Azimuth compression was then applied, followed by a coherent superposition of multistatic data to resolve aliasing effects and acquire a final SAS image.

Different approaches were also proposed by modifying some crucial steps in conventional RDA to achieve range-cell migration, range walk compensation or higher-order phase compensation. In [27], a second-order Wigner-Ville transform was applied to estimate the Doppler chirp rate. Motion compensation (MOCO), including range curvature correction and range walk (RW) compensation, could be achieved by using the Keystone transform, serving the purpose of RCMC

in conventional RDA. In [40], a range frequency reversal transform-fractional Fourier transform (RFRT-FrFT) method was proposed to estimate two SAR parameters, followed by MOCO with matched filtering, to focus the SAR image of ground moving target.

In this work, a multistatic synthetic aperture sonar (SAS) configuration, composed of a transceiver, a towed receiver and a stationary sonobuoy, is proposed to acquire focused images of a moving submarine as well as estimate its velocity vector from the Doppler centroids derived during the process. A monostatic imaging method is developed to process the signals at the transceiver, and a bistatic imaging method is developed to process the signals at the receiver and the sonobuoy, respectively. The time delay between transceiver/receiver/sonobuoy and target is incorporated under a non-stop-and-go premise, significantly reducing the image obscurity. The surface geometry of a 3D submarine model is adopted to simulate the backscattered signals from a real-world target. These features have only been sporadically disclosed in the literatures on SAS imaging.

The chirp rate in the range model is estimated by applying a range-frequency reversal transform (RFRT) and a modified second-order Wigner-Ville distribution (SoWVD) to the received signals, and the Doppler centroid in the range model is estimated by applying a Radon transform. Typical scenarios with the target moving in different directions and speeds are simulated to demonstrate the efficacy of the proposed approach. Three state-of-the-art methods are also used to verify the accuracy of the proposed method, the effects of noise are analyzed, and autofocus algorithms are applied to enhance the acquired images in some difficult cases.

This is the first article that provides a complete procedure on multistatic SAS imaging of moving submarines, as well as a rigorous method for estimate their velocity vector without prior knowledge. In this work, we explore the possibility of integrating a sonobuoy to increase the flexibility and versatility of SAS imaging and velocity estimation on underwater moving targets, which has never been discussed in the literature. This is the first work to propose the use of scan image projected from 3D target models to help verifying an acquired SAS image of a moving target and identifying it.

The rest of this work is organized as follows. The default parameters and the submarine model are elaborated in Section II, the imaging process in a monostatic and a bistatic SAS configurations are proposed in Sections III and IV, respectively. The method to estimate the velocity vector of the moving target is proposed in Section V. The acquired images in different scenarios are presented and discussed in Section VI, some important issues are further discussed in Section VII, and some conclusions are drawn in Section VIII.

II. SIMULATION SCENARIO

Fig.1 shows a multistatic configuration proposed to acquire SAS images of a moving target and estimate its velocity vector. A monostatic imaging method is developed to process the signals received at transceiver *A*, and a bistatic imaging method is developed to process the signals received at receiver *B* and sonobuoy *C*, respectively. The Doppler centroids derived from

processing the signals at A , B and C are used to estimate the velocity vector of the target.

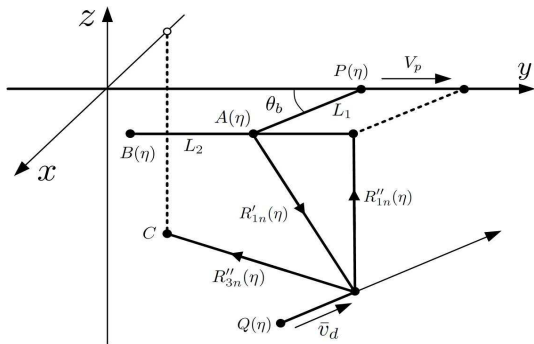


Fig. 1. SAS imaging on a moving point target, with transceiver A , receiver B and sonobuoy C in a multistatic configuration.

The transceiver A is cable-towed underwater by host ship P , moving in y direction at speed V_p . The receiver B is towed behind the transceiver, also moving in y direction at the same speed. The tow-cable of length $|PA| = L_1$ is laid at an angle θ_b about the y -axis, and the baseline length between A and B is $|AB| = L_2$. Thus, at slow time η , transceiver A is located at $(0, V_p\eta, -L_1 \sin \theta_b)$ and receiver B is located at $(0, V_p\eta - L_2, -L_1 \sin \theta_b)$. A passive receiver C is attached to a sonobuoy and is deposited at a fixed position of (x_C, y_C, z_C) . Sonar pulses are periodically emitted from transceiver A , and their echoes from the moving target are received later by A , B and C , respectively.

A. Default Parameters

TABLE I
DEFAULT PARAMETERS USED IN SIMULATIONS.

parameter	symbol	value	references
sound speed	c_s	1.5 km/s	[41]
platform velocity	V_p	3 m/s	[42], [43]
cable length	L_1	250 m	[44], [45]
baseline length	L_2	250 m	[44], [45]
tow-cable depression angle	θ_b	10°	[12], [44], [45]
carrier frequency	f_0	150 kHz	[13], [42]
range chirp rate	K_r	4 MHz/s	
pulse duration	T_r	5 ms	[13], [46]
range bandwidth	B_r	20 kHz	[13], [38]
range sampling rate	F_r	20 kHz	
pulse repetition frequency	F_a	80 Hz	
target exposure time	T_a	80 s	[47], [48]

Table I lists the default parameters used in the simulations. Typical military and commercial SAS systems move at speed of 1-3.5 m/s [42], [43], which is set to $V_p = 3$ m/s in the simulations. Typical length of towed cable is about 500 m, and the depth of towed sonar platform is about 50 m [12], [44], [45]. In the simulations, the cable length is set to $L_1 = 250$ m, the baseline is set to $L_2 = 250$ m, and the depression angle is set to $\theta_b = 10^\circ$, corresponding to a sonar depth of about 43 m. Receiver C is located at $(x_C, y_C, z_C) = (-500, 0, -150)$ m.

The carrier frequency ranges from few tens of kHz to 1 MHz in field testings [13], [38] or computer simulations [42],

[43], and is set to $f_0 = 150$ kHz in this work. The pulse duration varies from a few ms to 20 ms [13], [46], and is set to $T_r = 5$ ms. The range bandwidth varies from a few kHz to 40 kHz in field experiments [42] and computer simulations [13], and is set to $B_r = 20$ kHz. The synthetic aperture time runs from a few minutes to a few hours [47], [48], and is set to $T_a = 80$ s. The distance between the moving target and transceiver $A(\eta)$ at $\eta = 0$ is about 2 km. The longest possible echo spread from a submarine of 10 m in length is about 11.6 ms, when it moves in the cross-track direction. Thus, the pulse repetition frequency (PRF) is set to 80 Hz to avoid overlap of echoes from subsequent pulses.

B. Submarine Model

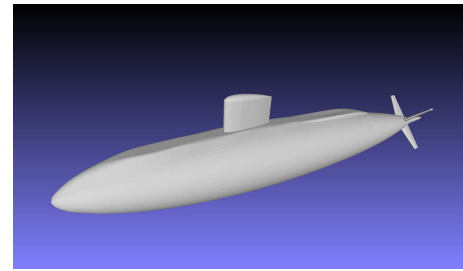


Fig. 2. Scale model of USS Albacore [49] used in the simulations.

Fig. 2 shows a scale model of the USS Albacore (AGSS-569), which was an auxiliary research submarine in service during 1953-1972 [49], having a length overall (LOA) of 62.13 m and maximum submerged speed of 25 knots (12.86 m/s). A model in [50] is adopted and tessellated with triangular meshes [51]. In the simulations, the Albacore model is scaled down in size by a factor of six, rendering an LOA of about 10 m.

In the field experiments of submarine prospecting and bathymetry, the maximum range varied from 150 to 350 m [42], [43], [46]. The range in the simulations is extended to about 2 km. To verify the proposed imaging methods in monostatic configuration in Section III and bistatic configuration in Section IV, the center of the scale submarine model is set to $(1, 989, 0, -350)$ m at $\eta = 0$ and moves with a velocity vector $\bar{v}_d = (v_x, v_y, v_z) = (0, -4, 0)$ m/s, opposite to the moving direction of the SAS platform.

III. MONOSTATIC IMAGING METHOD ON TRANSCEIVER SIGNALS

A. Range Model

The submarine model is tessellated with N_d flat patches, with each patch behaving as a scatterer. The ranges between transceiver A and the n th scatterer Q , with coordinates (x_{n0}, y_{n0}, z_{n0}) at $\eta = 0$, are $R'_{1n}(\eta)$ in the forward path and $R''_{1n}(\eta)$ in the backward path, with the explicit forms

$$R'_{1n}(\eta) \simeq R'_{10} + \frac{c_s f'_{dc1}}{2f_0} \eta + \frac{c_s K'_{a1}}{4f_0} \eta^2 \\ = R'_{10} + \Delta R'_{11}(\eta) + \Delta R'_{12}(\eta) \quad (1)$$

$$R''_{1n}(\eta) \simeq R''_{10} + \frac{c_s f''_{dc1}}{2f_0} \eta + \frac{c_s K''_{a1}}{4f_0} \eta^2 \\ = R''_{10} + \Delta R''_{11}(\eta) + \Delta R''_{12}(\eta) \quad (2)$$

where

$$R'_{10} = R'_{1n}(0) = \left[(x_{n0} + v_x R_{10}/c_s)^2 + (y_{n0} + v_y R_{10}/c_s)^2 + (z_{n0} + v_z R_{10}/c_s + L_1 \sin \theta_b)^2 \right]^{1/2}$$

$$R''_{10} = R''_{1n}(0) = \left\{ (x_{n0} + v_x R_{10}/c_s)^2 + (z_{n0} + v_z R_{10}/c_s + L_1 \sin \theta_b)^2 + [y_{n0} + (v_y - 2V_p) R_{10}/c_s]^2 \right\}^{1/2}$$

The associated Doppler centroids are given by

$$\begin{aligned} f'_{dc1} &= \frac{2f_0}{R'_{10} c_s} [v_x(x_{n0} + v_x R_{10}/c_s) + (v_y - V_p)(y_{n0} + v_y R_{10}/c_s) + v_z(z_{n0} + v_z R_{10}/c_s + L_1 \sin \theta_b)] \end{aligned} \quad (3)$$

$$\begin{aligned} f''_{dc1} &= \frac{2f_0}{R''_{10} c_s} [v_x(x_{n0} + v_x R_{10}/c_s) + (v_y - V_p)[y_{n0} + (v_y - 2V_p) R_{10}/c_s] + v_z(z_{n0} + v_z R_{10}/c_s + L_1 \sin \theta_b)] \end{aligned} \quad (4)$$

where

$$R_{10} = \sqrt{x_{n0}^2 + y_{n0}^2 + (z_{n0} + L_1 \sin \theta_b)^2}$$

is the range between A and Q at $\eta = 0$, under stop-and-go assumption, and the azimuth FM rates are given by

$$K'_{a1} = \frac{2f_0}{R'_{10} c_s} [v_x^2 + (v_y - V_p)^2 + v_z^2] \quad (5)$$

$$K''_{a1} = \frac{2f_0}{R''_{10} c_s} [v_x^2 + (v_y - V_p)^2 + v_z^2] \quad (6)$$

B. Range Compression

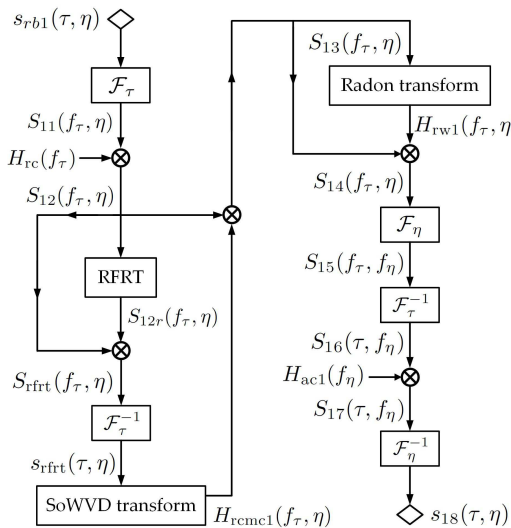


Fig. 3. Flow-chart of SAS imaging on a moving target in a monostatic configuration.

Fig.3 shows the flow-chart of the proposed SAS imaging method on a moving target in a monostatic configuration. A series of pulses are periodically emitted during an aperture

time T_a , each having a linear-frequency modulation (LFM) waveform of

$$s_t(\tau) = \text{rect}\left(\frac{\tau}{T_r}\right) e^{j2\pi f_0 \tau} e^{j\pi K_r \tau^2}$$

where τ is the fast time, T_r is the pulse duration, K_r is the chirp rate, f_0 is the carrier frequency, and

$$\text{rect}(t) = \begin{cases} 1, & |t| \leq 1/2 \\ 0, & \text{otherwise} \end{cases}$$

is a window function. The received signal at transceiver A after demodulation is given by

$$\begin{aligned} s_{rb1}(\tau, \eta) &= \sum_{n=1}^{N_d} A_n \text{rect}\left(\frac{\tau - [R'_{1n}(\eta) + R''_{1n}(\eta)]/c_s}{T_r}\right) \\ &\quad \text{rect}\left(\frac{\eta}{T_a}\right) e^{-j2\pi f_0 [R'_{1n}(\eta) + R''_{1n}(\eta)]/c_s} \\ &\quad e^{j\pi K_r (\tau - [R'_{1n}(\eta) + R''_{1n}(\eta)]/c_s)^2} \end{aligned} \quad (7)$$

where c_s is the acoustic speed in the ocean, A_n is the backscattering coefficient of the n th scatterer. Fig.4(a) shows the magnitude of $s_{rb1}(\tau, \eta)$.

Next, take the range Fourier transform of $s_{rb1}(\tau, \eta)$ to have

$$S_{11}(f_\tau, \eta) = \mathcal{F}_\tau\{s_{rb1}(\tau, \eta)\}$$

which is multiplied with a range compression (RC) filter [39]

$$H_{rc}(f_\tau) = e^{j\pi f_\tau^2 / K_r} \quad (8)$$

to obtain the range-compressed signal

$$\begin{aligned} S_{12}(f_\tau, \eta) &= S_{11}(f_\tau, \eta) H_{rc}(f_\tau) = \sum_{n=1}^{N_d} c_{11n} A_n \text{rect}\left(\frac{f_\tau}{B_r}\right) \\ &\quad \text{rect}\left(\frac{\eta}{T_a}\right) e^{-j2\pi(f_0+f_\tau)(R'_{11}+R''_{11})/c_s} \\ &\quad e^{-j2\pi(f_0+f_\tau)(\Delta R'_{11}(\eta)+\Delta R''_{11}(\eta))/c_s} \\ &\quad e^{-j2\pi(f_0+f_\tau)(\Delta R'_{12}(\eta)+\Delta R''_{12}(\eta))/c_s} \end{aligned} \quad (9)$$

C. Range Cell Migration Correction

The azimuth FM rate in the range-compressed signal is needed to correct range cell migration. We will first apply a range-frequency reversal transform (RFRT) [40] to concentrate the signal in $S_{12}(f_\tau, \eta)$ around a straight signal trace, then apply a modified second-order Wigner-Ville distribution (SoWVD) to estimate the azimuth FM rate.

To apply the RFRT, multiply $S_{12}(f_\tau, \eta)$ with its mirrored replica about f_τ to obtain

$$\begin{aligned} S_{rfrc}(f_\tau, \eta) &= S_{12}(f_\tau, \eta) S_{12}(-f_\tau, \eta) \\ &= \sum_{n=1}^{N_d} c_{11n}^2 A_n^2 \text{rect}\left(\frac{f_\tau}{B_r}\right) \text{rect}\left(\frac{\eta}{T_a}\right) \\ &\quad e^{-j4\pi f_0 (R'_1 + R''_1)/c_s} e^{-j4\pi f_0 (\Delta R'_{11}(\eta) + \Delta R''_{11}(\eta))/c_s} \\ &\quad e^{-j4\pi f_0 (\Delta R'_{12}(\eta) + \Delta R''_{12}(\eta))/c_s} \end{aligned} \quad (10)$$

which is inverse Fourier transformed in range to obtain

$$\begin{aligned} s_{\text{rftr}}(\tau, \eta) &= \mathcal{F}_\tau^{-1}\{S_{\text{rftr}}(f_\tau, \eta)\} \\ &= \sum_{n=1}^{N_d} c_{11n}^2 A_n^2 \text{sinc}(B_r \tau) \text{rect}\left(\frac{\eta}{T_a}\right) \\ &\quad e^{-j4\pi f_0(R'_{10} + R''_{10})/c_s} e^{-j4\pi f_0(\Delta R'_{11}(\eta) + \Delta R''_{11}(\eta))/c_s} \\ &\quad e^{-j4\pi f_0(\Delta R'_{12}(\eta) + \Delta R''_{12}(\eta))/c_s} \end{aligned} \quad (11)$$

Fig.5(a) shows the magnitude of $s_{\text{rftr}}(\tau, \eta)$, which is concentrated within a few range cells around $\tau = 0$. The range cell migration and range walk have been simultaneously compensated, manifested by the absence of τ - η coupling terms in (11).

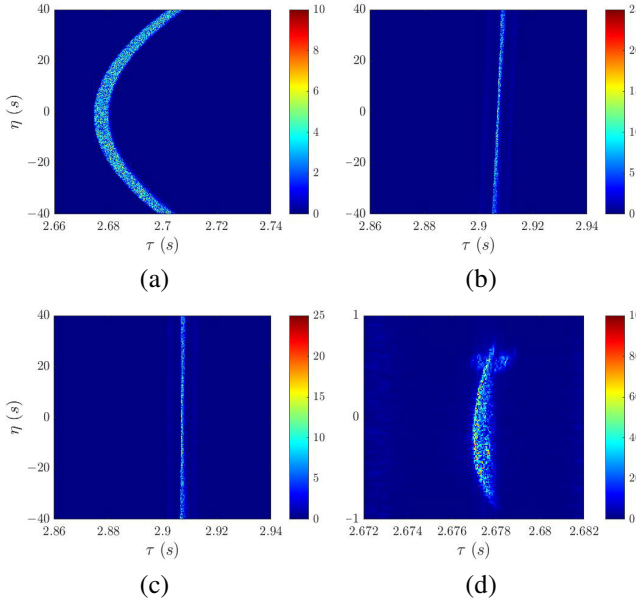


Fig. 4. Magnitude of (a) $s_{\text{rb}1}(\tau, \eta)$, (b) $s_{\text{rcmc}1}(\tau, \eta)$, (c) $s_{\text{rw}1}(\tau, \eta)$, (d) $s_{18}(\tau, \eta)$.

Define a modified second-order Wigner-Ville distribution (SoWVD) of $s_{\text{rftr}}(\tau_0, \eta)$ as [27]

$$s_{\text{wv}}(p, \eta) = s_{\text{rftr}}(\tau_0, \eta + p/2) s_{\text{rftr}}^*(\tau_0, \eta - p/2) [s_{\text{rftr}}(\tau_0, \eta + p/2 + p_0) s_{\text{rftr}}^*(\tau_0, \eta - p/2 - p_0)]^* \quad (12)$$

By taking the Fourier transform of $s_{\text{wv}}(p, \eta)$ with respect to both p and η , we obtain

$$S_{\text{wv}}(f_p, f_\eta) = \mathcal{F}_p \{ \mathcal{F}_\eta \{ s_{\text{wv}}(p, \eta) \} \} \quad (13)$$

where p_0 is a tuning parameter to achieve tradeoff between the focus area in the $f_p f_\eta$ plane and the resolution in f_η .

By substituting (11) into (12), we have

$$\begin{aligned} s_{\text{wv}}(p, \eta) &= \sum_{n=1}^{N_d} |c_{11n}|^8 |A_n|^8 \\ &\quad \text{rect}\left(\frac{\eta}{T_a}\right) e^{j8\pi p_0 f_{dc1,eq}} e^{j8\pi p_0 \eta K_{a1,eq}} \end{aligned}$$

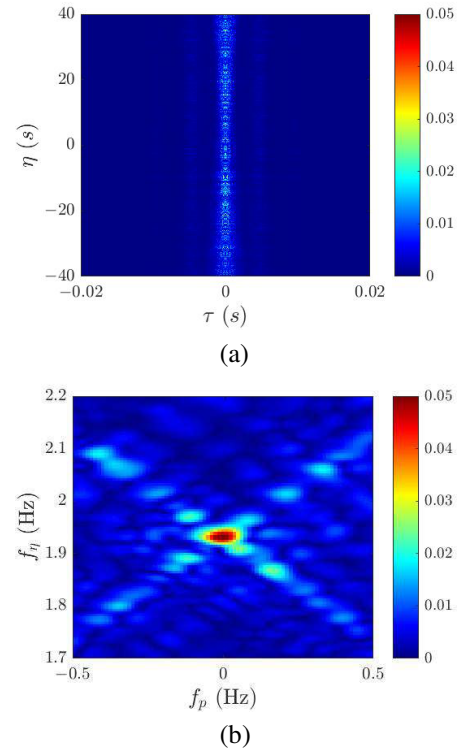


Fig. 5. Magnitude of (a) $s_{\text{rftr}}(\tau, \eta)$, (b) $S_{\text{wv}}(f_p, f_\eta)$.

which is substituted into (13) to obtain

$$S_{\text{wv}}(f_p, f_\eta) = \sum_{n=1}^{N_d} |c_{11n}|^8 |A_n|^8 \text{sinc}[T_a(f_\eta - 4p_0 K_{a1,eq})] \delta(f_p) e^{j8\pi p_0 f_{dc1,eq}} \quad (14)$$

where

$$f_{dc1,eq} = (f'_{dc1} + f''_{dc1})/2 \quad (15)$$

$$K_{a1,eq} = (K'_{a1} + K''_{a1})/2 \quad (16)$$

Fig.5(b) shows the magnitude of $S_{\text{wv}}(f_p, f_\eta)$, manifesting a peak at $(f_p, f_\eta) = (0, \tilde{f}_\eta) = (0, 1.934)$ Hz. By relating the peak with the argument of sinc function in (14), the azimuth FM rate is estimated as $\tilde{K}_{a1,eq} = 4.834$ Hz/s, which is close to the true value of $K_{a1,eq} = 4.879$ Hz/s.

Next, design an RCMC filter, with the estimated value of $K_{a1,eq}$ defined in (16), as

$$H_{\text{rcmc}1}(f_\tau, \eta) = e^{j\pi f_\tau \tilde{K}_{a1,eq} \eta^2 / f_0}$$

Multiply it with $S_{12}(f_\tau, \eta)$ in (9) to obtain

$$S_{13}(f_\tau, \eta) = S_{12}(f_\tau, \eta) H_{\text{rcmc}1}(f_\tau, \eta)$$

which is inverse Fourier transformed in range to have

$$\begin{aligned} s_{\text{rcmc}1}(\tau, \eta) &= \mathcal{F}_\tau^{-1}\{S_{13}(f_\tau, \eta)\} \\ &= \sum_{n=1}^{N_d} c_{11n} A_n \text{rect}\left(\frac{\eta}{T_a}\right) e^{-j4\pi f_0 R_{1n}(\eta)/c_s} \\ &\quad \text{sinc}\left\{B_r \left[\tau - \frac{R'_{10} + R''_{10}}{c_s} - \frac{f_{dc1,eq}}{f_0} \eta\right]\right\} \end{aligned} \quad (17)$$

Fig.4(b) shows the magnitude of $s_{\text{rcmc}1}(\tau, \eta)$, revealing oblique lines.

D. Range Walk Compensation and Image Focusing

The argument of sinc function in (17) indicates a line equation in the τ - η plane

$$\tau - \frac{f_{dc1,eq}}{f_0} \eta = \frac{R'_{10} + R''_{10}}{c_s}$$

with slope

$$\tan \theta_R = -f_{dc1,eq}/f_0$$

which can be estimated by applying a Radon transform to $|s_{rcmc1}(\tau, \eta)|$, leading to $f_{dc1,eq} \simeq 5.772$ Hz, which is close to the true value of $f_{dc1,eq} = 6.533$ Hz.

Eqns.(1), (2) and (15) imply that

$$\Delta R'_{11}(\eta) + \Delta R''_{11}(\eta) = -c_s \tan \theta_R \eta$$

The phase term $e^{-j2\pi(f_0+f_\tau)(\Delta R'_{11}(\eta)+\Delta R''_{11}(\eta))/c_s}$ embedded in $S_{13}(f_\tau, \eta)$, accounting for the range-walk effect, can be compensated by multiplying $S_{13}(f_\tau, \eta)$ with a range-walk filter

$$H_{rw1}(f_\tau, \eta) = e^{-j2\pi(f_0+f_\tau)\tan \theta_R \eta}$$

to have

$$S_{14}(f_\tau, \eta) = S_{13}(f_\tau, \eta) H_{rw1}(f_\tau, \eta)$$

of which the inverse Fourier transform in range is

$$\begin{aligned} s_{rw1}(\tau, \eta) &= \mathcal{F}_\tau^{-1}\{S_{14}(f_\tau, \eta)\} \\ &= \sum_{n=1}^{N_d} c_{11n} A_n \text{sinc}\left(\tau - \frac{R'_{10} + R''_{10}}{c_s}\right) \text{rect}\left(\frac{\eta}{T_a}\right) \\ &\quad e^{-j2\pi f_0(R'_{10} + R''_{10} + \Delta R'_{12}(\eta) + \Delta R''_{12}(\eta))/c_s} \end{aligned}$$

Fig.4(c) shows the magnitude of $s_{rw1}(\tau, \eta)$, revealing straight lines parallel to the azimuth axis.

Next, take the azimuth Fourier transform of $S_{14}(f_\tau, \eta)$ to have

$$S_{15}(f_\tau, f_\eta) = \mathcal{F}_\eta\{S_{14}(f_\tau, \eta)\}$$

which is inverse Fourier transformed in range to have

$$\begin{aligned} S_{16}(\tau, f_\eta) &= \mathcal{F}_\tau^{-1}\{S_{15}(f_\tau, f_\eta)\} \\ &= \sum_{n=1}^{N_d} c_{12n} c_{11n} A_n \text{rect}\left(\frac{f_\eta}{B_{a1}}\right) e^{j\pi f_\eta^2/K_{a1,eq}} \\ &\quad \text{sinc}\left[B_r\left(\tau - \frac{R'_{10} + R''_{10}}{c_s}\right)\right] e^{-j2\pi f_0(R'_{10} + R''_{10})/c_s} \quad (18) \end{aligned}$$

where $B_{a1} = K_{a1,eq} T_a$ is the azimuth bandwidth, and the argument of sinc function indicates focusing in range.

Design an azimuth compression (AC) filter [39]

$$H_{ac1}(f_\eta) = e^{-j\pi f_\eta^2/\tilde{K}_{a1,eq}} \quad (19)$$

which is multiplied with $S_{16}(\tau, f_\eta)$ to have

$$S_{17}(\tau, f_\eta) = S_{16}(\tau, f_\eta) H_{ac1}(f_\eta)$$

where the second-order phase term in (18) has been compensated. Finally, take the inverse Fourier transform of $S_{17}(\tau, f_\eta)$ in azimuth to have

$$\begin{aligned} s_{18}(\tau, \eta) &= \mathcal{F}_\eta^{-1}\{S_{17}(\tau, f_\eta)\} \\ &= \sum_{n=1}^{N_d} c_{12n} c_{11n} A_n e^{-j2\pi f_0(R'_{10} + R''_{10})/c_s} \\ &\quad \text{sinc}\left[B_r\left(\tau - \frac{R'_{10} + R''_{10}}{c_s}\right)\right] \text{sinc}(B_{a1}\eta) \quad (20) \end{aligned}$$

where the argument of sinc function in η indicates focusing in azimuth. Fig.4(d) shows the final image of the moving target, which is well focused.

IV. BISTATIC IMAGING METHOD ON RECEIVER SIGNALS

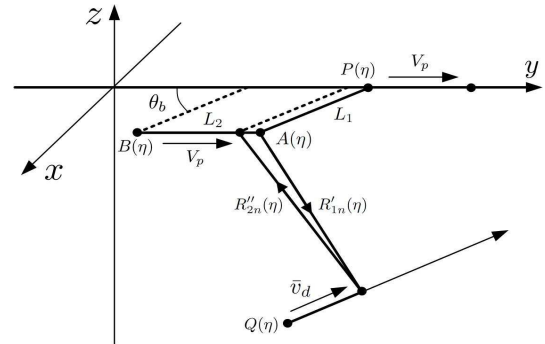


Fig.6. Range model of SAS imaging on a moving point target with receiver B in a bistatic configuration.

Fig.6 shows the range model of SAS imaging on a moving point target with receiver B in a bistatic configuration. The range between receiver B and the n th scatterer Q is given by

$$\begin{aligned} R''_{2n}(\eta) &\simeq R''_{20} + \frac{c_s f''_{dc2}}{2f_0} \eta + \frac{c_s K''_{a2}}{4f_0} \eta^2 \\ &= R''_{20} + \Delta R''_{21}(\eta) + \Delta R''_{22}(\eta) \quad (21) \end{aligned}$$

with

$$\begin{aligned} R''_{20} &= R''_{20}(0) = \left\{ (x_{n0} + v_x R_{10}/c_s)^2 \right. \\ &\quad + (z_{n0} + v_z R_{10}/c_s + L_1 \sin \theta_b)^2 \\ &\quad \left. + [y_{n0} + L_2 + (v_y - V_p) R_{10}/c_s - V_p R_{20}/c_s]^2 \right\}^{1/2} \quad (22) \end{aligned}$$

The Doppler centroid is given by

$$\begin{aligned} f''_{dc2} &= \frac{2f_0}{R''_{20} c_s} \{v_x(x_{n0} + v_x R_{10}/c_s) \\ &\quad + (v_y - V_p)[y_{n0} + L_2 + (v_y - V_p) R_{10}/c_s - V_p R_{20}/c_s] \\ &\quad + v_z(z_{n0} + v_z R_{10}/c_s + L_1 \sin \theta_b)\} \quad (23) \end{aligned}$$

where

$$R_{20} = \sqrt{x_{n0}^2 + (z_{n0} + L_1 \sin \theta_b)^2 + (y_{n0} + L_2)^2} \quad (24)$$

is the range between receiver B and Q at $\eta = 0$, and the azimuth FM rate is given by

$$K''_{a2} = \frac{2f_0[v_x^2 + (v_y - V_p)^2 + v_z^2]}{R''_{20} c_s} \quad (25)$$

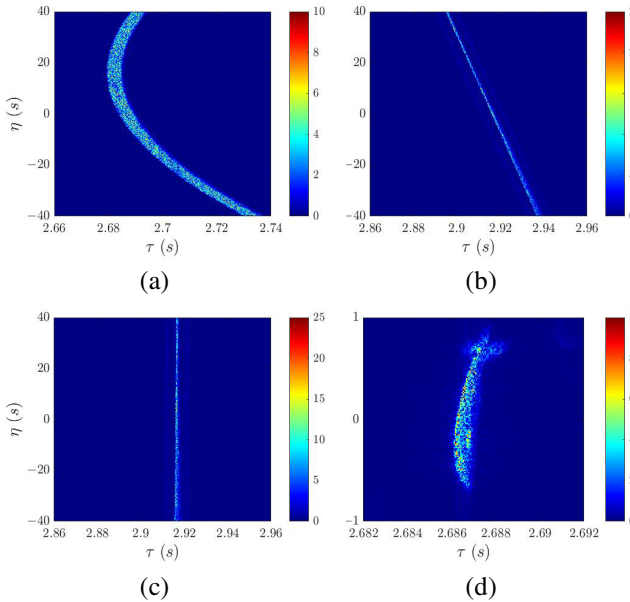


Fig. 7. Magnitude of (a) $s_{rb2}(\tau, \eta)$, (b) $s_{rcmc2}(\tau, \eta)$, (c) $s_{rw2}(\tau, \eta)$, (d) $s_{2s}(\tau, \eta)$.

To apply range compression to $s_{rb2}(\tau, \eta)$, first take the range Fourier transform of $s_{rb2}(\tau, \eta)$ to have

$$S_{21}(f_\tau, \eta) = \mathcal{F}_\tau\{s_{rb2}(\tau, \eta)\}$$

which is multiplied with the range-compression filter in (8) to have

$$\begin{aligned} S_{22}(f_\tau, \eta) &= \sum_{n=1}^{N_d} c_{21n} A_{n2} \text{rect}\left(\frac{f_\tau}{B_r}\right) \text{rect}\left(\frac{\eta}{T_a}\right) \\ &\quad e^{-j2\pi(f_0+f_\tau)(R'_{10}+R''_{20})/c_s} e^{-j2\pi(f_0+f_\tau)[\Delta R'_{11}(\eta)+\Delta R''_{21}(\eta)]/c_s} \\ &\quad \exp\left\{-j\frac{\pi(f_0+f_\tau)}{f_0} K_{a2,eq} \eta^2\right\} \end{aligned} \quad (26)$$

where

$$K_{a2,eq} = (K'_{a1} + K''_{a2})/2$$

To conduct range cell migration correction, first apply the range-frequency reversal transform (RFRT) defined in (10) to $S_{22}(f_\tau, \eta)$, obtaining another $S_{rfrt}(f_\tau, \eta)$, which is inverse Fourier transformed in range to obtain $s_{rfrt}(\tau, \eta)$. Then, form a modified second-order Wigner-Ville distribution of $s_{rfrt}(\tau_0, \eta)$, defined in (12), as $s_{wv}(p, \eta)$, which is Fourier transformed to obtain

$$S_{wv}(f_p, f_\eta) = \mathcal{F}_p\{\mathcal{F}_\eta\{s_{wv}(p, \eta)\}\}$$

The peak of $|S_{wv}(f_p, f_\eta)|$ appears at $\tilde{f}_\eta = 1.921$ Hz, implying that $\tilde{K}_{a2,eq} \simeq 4.803$ Hz/s, which is close to the true value of $K_{a2,eq} = 4.863$ Hz/s.

The value of $\tilde{K}_{a2,eq}$ is used to design an RCMC filter

$$H_{rcmc2}(f_\tau, \eta) = e^{j\pi f_\tau \tilde{K}_{a2,eq} \eta^2/f_0}$$

which is multiplied with (26) to obtain

$$\begin{aligned} S_{23}(f_\tau, \eta) &= S_{22}(f_\tau, \eta) H_{rcmc2}(f_\tau, \eta) \\ &\simeq \sum_{n=1}^{N_d} c_{21n} A_{n2} \text{rect}\left(\frac{f_\tau}{B_r}\right) \text{rect}\left(\frac{\eta}{T_a}\right) \\ &\quad e^{-j2\pi(f_0+f_\tau)[R'_{10}+R''_{20}+\Delta R'_{11}(\eta)+\Delta R''_{21}(\eta)]/c_s} \\ &\quad e^{-j2\pi f_0[\Delta R'_{12}(\eta)+\Delta R''_{22}(\eta)]/c_s} \end{aligned}$$

Then, take the inverse Fourier transform of $S_{23}(f_\tau, \eta)$ in range to have

$$\begin{aligned} s_{rcmc2}(\tau, \eta) &= \mathcal{F}_\tau^{-1}\{S_{23}(f_\tau, \eta)\} \\ &= \sum_{n=1}^{N_d} c_{21n} A_{n2} \text{rect}\left(\frac{\eta}{T_a}\right) e^{-j2\pi f_0[R'_{1n}(\eta)+R''_{2n}(\eta)]/c_s} \\ &\quad \text{sinc}\left[B_r\left(\tau - \frac{R'_{10}+R''_{20}}{c_s} - \frac{f'_{dc1}+f''_{dc2}}{2f_0}\eta\right)\right] \end{aligned} \quad (27)$$

Fig.7(b) shows the magnitude of $s_{rcmc2}(\tau, \eta)$, revealing oblique lines.

The argument of sinc function in (27) indicates a line equation in the τ - η plane,

$$\tau - \frac{R'_{10}+R''_{20}}{c_s} - \frac{f_{dc2,eq}}{f_0}\eta = 0$$

of which the slope is related to

$$f_{dc2,eq} = (f'_{dc1} + f''_{dc2})/2 \quad (28)$$

The slope is estimated by applying the Radon transform to $|s_{rcmc2}(\tau, \eta)|$, leading to $f_{dc2,eq} \simeq -80.092$ Hz, which is close to the true value of $f_{dc2,eq} = -80.022$ Hz. The estimated slope is then used to design a range-walk filter

$$H_{rw2}(f_\tau, \eta) = e^{j2\pi(f_0+f_\tau)\tan\tilde{\theta}_R\eta}$$

which is multiplied with $S_{23}(f_\tau, \eta)$ to compensate the range walk as

$$S_{24}(f_\tau, \eta) = S_{23}(f_\tau, \eta) H_{rw2}(f_\tau, \eta)$$

Then, take the inverse Fourier transform of $S_{24}(f_\tau, \eta)$ in range to have

$$\begin{aligned} s_{rw2}(\tau, \eta) &= \mathcal{F}_\tau^{-1}\{S_{24}(f_\tau, \eta)\} \\ &= \sum_{n=1}^{N_d} c_{21n} A_{n2} \text{sinc}\left(\tau - \frac{R'_{10}+R''_{20}}{c_s}\right) \text{rect}\left(\frac{\eta}{T_a}\right) \\ &\quad e^{-j2\pi f_0[R'_{10}+R''_{20}+\Delta R'_{12}(\eta)+\Delta R''_{22}(\eta)]/c_s} \end{aligned}$$

Fig.7(c) shows the magnitude of $s_{rw2}(\tau, \eta)$, revealing straight lines parallel to the azimuth axis.

Next, take the azimuth Fourier transform of $S_{24}(f_\tau, \eta)$ to have

$$S_{25}(f_\tau, f_\eta) = \mathcal{F}_\eta\{S_{24}(f_\tau, \eta)\} \quad (29)$$

which is inverse Fourier transformed in range to have

$$\begin{aligned} S_{26}(\tau, f_\eta) &= \mathcal{F}_\tau^{-1}\{S_{25}(f_\tau, f_\eta)\} \\ &= \sum_{n=1}^{N_d} c_{22n} c_{21n} A_{n2} \text{rect}\left(\frac{f_\eta}{B_{a2}}\right) e^{j\pi f_\eta^2/K_{a2,eq}} \\ &\quad \text{sinc}\left[B_r\left(\tau - \frac{R'_{10}+R''_{20}}{c_s}\right)\right] e^{-j2\pi f_0(R'_{10}+R''_{20})/c_s} \end{aligned} \quad (30)$$

where the argument of the sinc function in τ indicates focusing in range.

Next, design an azimuth-compression filter with the estimated value of $\tilde{K}_{a2,eq}$ [39]

$$H_{ac2}(f_\eta) = e^{-j\pi f_\eta^2 / \tilde{K}_{a2,eq}} \quad (31)$$

which is multiplied with $S_{26}(\tau, f_\eta)$ to compensate the second-order phase term as

$$S_{27}(\tau, f_\eta) = S_{26}(\tau, f_\eta) H_{ac2}(f_\eta)$$

Finally, take the inverse azimuth Fourier transform of $S_{27}(\tau, f_\eta)$ to have

$$\begin{aligned} s_{28}(\tau, \eta) &= \mathcal{F}_\eta^{-1}\{S_{27}(\tau, f_\eta)\} \\ &= \sum_{n=1}^{N_d} c_{22n} c_{21n} A_{n2} e^{-j2\pi f_0(R'_{10} + R''_{20})/c_s} \\ &\quad \text{sinc} \left[B_r \left(\tau - \frac{R'_{10} + R''_{20}}{c_s} \right) \right] \text{sinc}(B_{a2}\eta) \end{aligned}$$

where the argument of sinc function in η indicates focusing in azimuth. Fig.7(d) shows the final image of the moving target, which is well focused.

Similar to (21), (22), (23) and (24), the range between receiver C and the n th scatterer is given by

$$\begin{aligned} R''_{3n}(\eta) &= \{[(x_{n0} + v_x\eta + v_x\Delta t_d) - x_C]^2 \\ &\quad + [(y_{n0} + v_y\eta + v_y\Delta t_d) - y_C]^2 \\ &\quad + [(z_{n0} + v_z\eta + v_z\Delta t_d) - z_C]^2\}^{1/2} \\ &\simeq R''_{30} + \frac{c_s f''_{dc3}}{2f_0} \eta + \frac{c_s K''_{a3}}{4f_0} \eta^2 \\ &= R''_{30} + \Delta R''_{31}(\eta) + \Delta R''_{32}(\eta) \end{aligned}$$

where

$$\begin{aligned} R''_{30} &= R''_{3n}(0) = \{(x_{n0} + v_x\Delta t_d - x_C)^2 \\ &\quad + (y_{n0} + v_y\Delta t_d - y_C)^2 + (z_{n0} + v_z\Delta t_d - z_C)^2\}^{1/2} \end{aligned}$$

and the Doppler centroid is given by

$$\begin{aligned} f''_{dc3} &= \frac{2f_0}{R''_{30}c_s} \{v_x(x_{n0} + v_xR_{10}/c_s - x_C) \\ &\quad + v_y(y_{n0} + v_yR_{10}/c_s - y_C) \\ &\quad + v_z(z_{n0} + v_zR_{10}/c_s - z_C)\} \quad (32) \end{aligned}$$

A final image, $s_{38}(\tau, \eta)$, is acquired by applying the same imaging method proposed in this Section that leads to $s_{28}(\tau, \eta)$.

V. ESTIMATION OF TARGET VELOCITY VECTOR

Although the target shown in Figs.4(d) and 7(d) are well focused, its size and moving direction are indeterminate yet. In this Section, a semi-analytic method is proposed to estimate the target velocity vector. By substituting (3) and (4) into (15),

the Doppler centroids observed at transceiver A is related to the motion parameters of the target as

$$\begin{aligned} f_{dc1,eq}(\bar{v}_d) &= \frac{f_0}{R'_{10}c_s} [v_x(x_{n0} + v_xR_{10}/c_s) \\ &\quad + (v_y - V_p)(y_{n0} + v_yR_{10}/c_s) \\ &\quad + v_z(z_{n0} + v_zR_{10}/c_s + L_1 \sin \theta_b)] \\ &\quad + \frac{f_0}{R''_{10}c_s} \{v_x(x_{n0} + v_xR_{10}/c_s) \\ &\quad + (v_y - V_p)[y_{n0} + L_2 + (v_y - 2V_p)R_{10}/c_s] \\ &\quad + v_z(z_{n0} + v_zR_{10}/c_s + L_1 \sin \theta_b)\} \quad (33) \end{aligned}$$

Similarly, by substituting (3) and (23) into (28), the Doppler centroids observed at receiver B is given by

$$\begin{aligned} f_{dc2,eq}(\bar{v}_d) &= \frac{f_0}{R'_{10}c_s} [v_x(x_{n0} + v_xR_{10}/c_s) \\ &\quad + (v_y - V_p)(y_{n0} + v_yR_{10}/c_s) \\ &\quad + v_z(z_{n0} + v_zR_{10}/c_s + L_1 \sin \theta_b)] \\ &\quad + \frac{f_0}{R''_{20}c_s} \{v_x(x_{n0} + v_xR_{10}/c_s) \\ &\quad + (v_y - V_p)[y_{n0} + L_2 + (v_y - V_p)R_{10}/c_s - V_pR_{20}/c_s] \\ &\quad + v_z(z_{n0} + v_zR_{10}/c_s + L_1 \sin \theta_b)\} \quad (34) \end{aligned}$$

A third equation of Doppler centroids observed at receiver C is derived, by using (3) and (32), as

$$\begin{aligned} f_{dc3,eq}(\bar{v}_d) &= \frac{f'_{dc1} + f''_{dc3}}{2} = \frac{f_0}{R'_{10}c_s} \{[v_x(x_{n0} + v_xR_{10}/c_s)] \\ &\quad + [(v_y - V_p)(y_{n0} + v_yR_{10}/c_s)] \\ &\quad + [v_z(z_{n0} + v_zR_{10}/c_s + L_1 \sin \theta_b)]\} \\ &\quad + \frac{f_0}{R''_{30}c_s} \{v_x(x_{n0} + v_xR_{10}/c_s - x_C) \\ &\quad + v_y(y_{n0} + v_yR_{10}/c_s - y_C) \\ &\quad + v_z(z_{n0} + v_zR_{10}/c_s - z_C)\} \quad (35) \end{aligned}$$

Eqns.(33), (34) and (35) specify three two-dimensional surfaces in the three-dimensional $v_x v_y v_z$ space, with the true velocity vector $\bar{v}_d = (v_x, v_y, v_z)$ residing at the intersection of these three surfaces. By applying Radon transform to $s_{rcmc1}(\tau, \eta)$ in (17), derived from the backscattered signals at transceiver A , $f_{dc1,eq}$ is estimated as $\tilde{f}_{dc1,eq}$. Similarly, $f_{dc2,eq}$ is estimated as $\tilde{f}_{dc2,eq}$ by applying Radon transform to $s_{rcmc2}(\tau, \eta)$ in (27), derived from the backscattered signals at receiver B , and $f_{dc3,eq}$ is estimated as $\tilde{f}_{dc3,eq}$ from the backscattered signals at receiver C .

To solve (33), (34) and (35) numerically, first define a 3D grid in (v_x, v_y, v_z) at uniform spacing of Δv . At each grid point, compute the difference between the estimated value $\tilde{f}_{dc\alpha,eq}$ and $f_{dc\alpha,eq}(\bar{v}_d)$ determined with (33), (34) or (35) as

$$\chi_\alpha(\bar{v}_d) = f_{dc\alpha,eq}(\bar{v}_d) - \tilde{f}_{dc\alpha,eq}$$

where $\alpha = 1, 2, 3$. A grid-search method is then applied to look for \bar{v}_d that satisfies

$$\chi_1(\bar{v}_d) = \chi_2(\bar{v}_d) = \chi_3(\bar{v}_d) = 0$$

Fig.8 shows the solution surfaces of $\chi_1 = 0$, $\chi_2 = 0$ and $\chi_3 = 0$, respectively, in case 1. Their intersection point is the estimated velocity vector \tilde{v}_d .

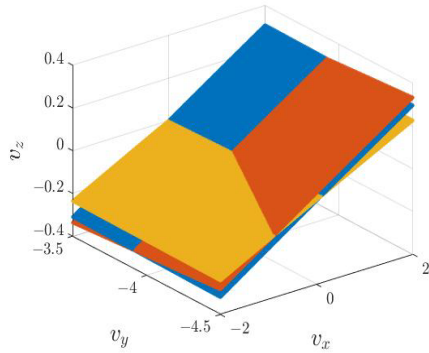


Fig. 8. Solution surfaces in case 1, $\chi_1 = 0$ (blue), $\chi_2 = 0$ (orange), $\chi_3 = 0$ (yellow).

VI. GENERAL DISCUSSIONS ON IMAGING RESULTS

TABLE II
TRUE AND ESTIMATED PARAMETERS OF MOVING TARGET.

	case 1	case 2	case 3	case 4
v_x (m/s)	0	0	0	0
v_y (m/s)	-4.0	4.0	-5.0	-5.0
v_z (m/s)	0	0	3.0	-3.0
$\tau_{c1,eq}$ (s)	2.677	2.677	2.677	2.678
$\eta_{c1,eq}$ (s)	0	0	0.1	-0.3
$f_{dc1,eq}$ (Hz)	6.355	0.077	-81.907	99.817
$\tau_{c2,eq}$ (s)	2.687	2.688	2.686	2.687
$\eta_{c2,eq}$ (s)	0	0	0.25	0
$f_{dc2,eq}$ (Hz)	-79.476	12.390	-179.539	1.626
$\tau_{c3,eq}$ (s)	3.000	3.000	3.000	3.001
$\eta_{c3,eq}$ (s)	0	0	0	-0.3
$f_{dc3,eq}$ (Hz)	2.583	0.917	-65.049	74.036
\tilde{v}_x (m/s)	0.002	-0.020	-0.050	0.033
\tilde{v}_y (m/s)	-3.914	3.992	-4.886	-4.890
\tilde{v}_z (m/s)	0.000	-0.003	2.993	-2.996
$ \Delta\bar{v}_d $ (m/s)	0.086	0.022	0.125	0.115
$100\frac{ \Delta\bar{v}_d }{ \bar{v}_d }(\%)$	2.151	0.550	2.144	1.972
	case 5	case 6	case 7	case 8
v_x (m/s)	1.5	3.0	0	3.0
v_y (m/s)	8.0	-5.0	3.0	0
v_z (m/s)	1.0	3.0	0	0
$\tau_{c1,eq}$ (s)	2.680	2.682	2.677	2.681
$\eta_{c1,eq}$ (s)	-0.2	-11.5	-	-1.1
$f_{dc1,eq}$ (Hz)	268.134	503.602	0	593.264
$\tau_{c2,eq}$ (s)	2.690	2.691	2.687	2.691
$\eta_{c2,eq}$ (s)	-0.3	-11.3	-	-1.1
$f_{dc2,eq}$ (Hz)	328.833	403.319	0	554.189
$\tau_{c3,eq}$ (s)	3.003	3.005	3.000	3.004
$\eta_{c3,eq}$ (s)	-0.4	-1.0	0	-1.9
$f_{dc3,eq}$ (Hz)	278.644	526.257	0.409	594.629
\tilde{v}_x (m/s)	1.318	3.124	-0.010	2.918
\tilde{v}_y (m/s)	7.992	-4.963	3.000	-0.011
\tilde{v}_z (m/s)	0.960	3.011	-0.002	0.017
$ \Delta\bar{v}_d $ (m/s)	0.187	0.130	0.010	0.084
$100\frac{ \Delta\bar{v}_d }{ \bar{v}_d }(\%)$	2.280	1.982	0.333	2.800

In this Section, eight typical cases of target moving in different directions and at different speeds are simulated. Table II lists the parameters in these cases, including the true velocity vector, center coordinates of target ($\tau_{cn,eq}, \eta_{cn,eq}$), Doppler centroid $f_{dcn,eq}$, with $n = 1, 2, 3$, the estimated velocity vector, the error of velocity vector $\Delta\bar{v}_d = \tilde{v}_d - \bar{v}_d$ (m/s), and

the percentage error of velocity, defined as $100 \times |\Delta\bar{v}_d|/|\bar{v}_d|$ (%).

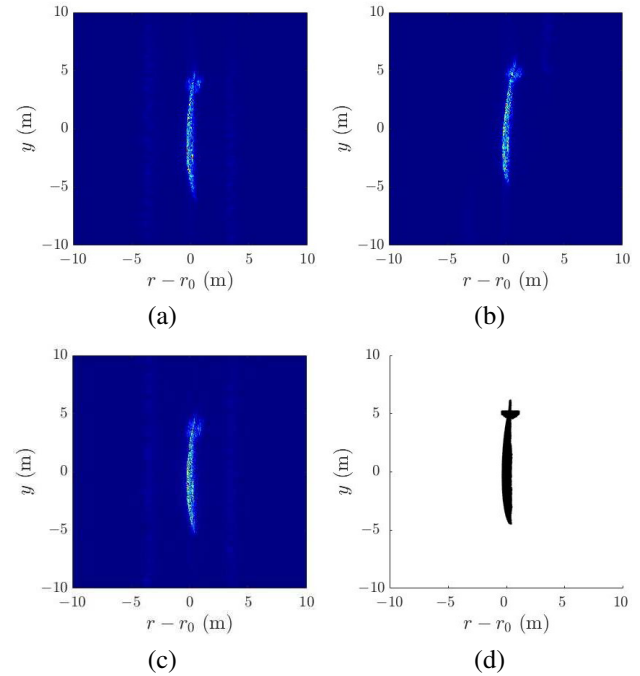


Fig. 9. SAS images in case 1, acquired from signals at (a) transceiver A, (b) receiver B, (c) receiver C; (d) scan image of target model.

Fig.9 shows the SAS images acquired in case 1, with the submarine moving in opposite direction to transceiver A, bearing no sway or heave motions. The SAS images are transformed from the $\tau\eta$ plane to an ry plane as

$$r = c_s \tau / 2$$

$$y = (V_p - \tilde{v}_y)(\eta - \eta_{c,eq})$$

where $\tau_{c,eq}$ and $\eta_{c,eq}$ are the fast time and slow time, respectively, at the closest range, and the image is centered at $r = r_0 = c_s \tau_{c,eq} / 2$ and $y = y_0 = -(V_p - \tilde{v}_y)\eta_{c,eq}$. Note that the platform velocity is comparable to the target velocity in SAS imaging.

Figs.9(a), 9(b) and 9(c) show the SAS images transformed from $s_{18}(\tau, \eta)$, $s_{28}(\tau, \eta)$ and $s_{38}(\tau, \eta)$, respectively. Fig.9(d) shows a scan image derived by projecting the scale model in Fig.2 from the xyz coordinates onto the ry plane, perceived from transceiver A. The scan image bears resemblance to the three SAS images.

Figs.9(a)-9(c) show that the scattered signals from the submarine hull are relatively strong, the shape and position of the sail is barely discernible. The signals scattered from the sail is relatively weak and are mixed with those from the hull. The signals scattered from the rudders and propellers near the stern are relatively weak, but their shapes are still discernible.

Figs.10(a)-10(c) show the SAS images in case 2, acquired with the received signals at transceiver A, receiver B and receiver C, respectively. The submarine moves slightly faster than the SAS platform in the same direction, bearing no sway or heave motions. Fig.10(d) shows the scan image viewed from transceiver A, which matches well in size and shape

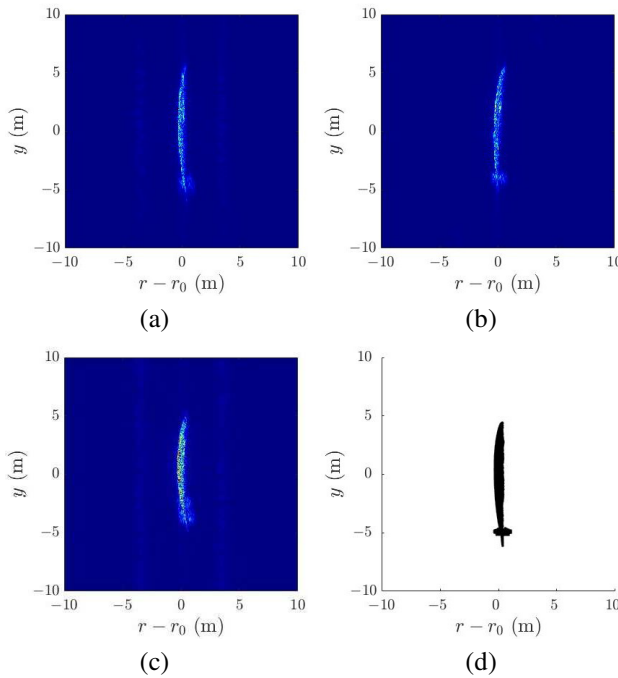


Fig. 10. SAS images in case 2, acquired from signals at (a) transceiver A, (b) receiver B, (c) receiver C; (d) scan image of target model.

with the three SAS images. The images in Figs.10(a)-10(c) reveal similar features to their counterparts in case 1. The scattered signals from the submarine hull are stronger than those scattered from the sail. The signals scattered from the rudders and propellers are even weaker, but their features are recognizable. The images in these two cases are reversed in y direction, consistent with the target moving direction.

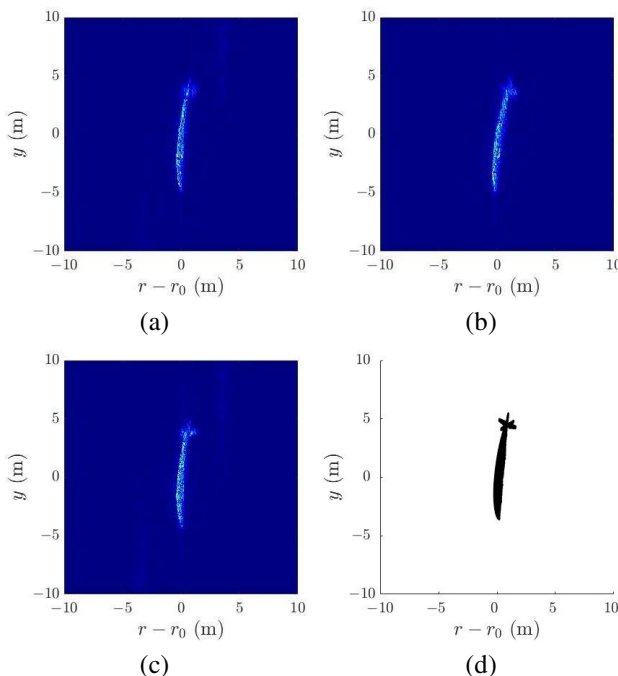


Fig. 11. SAS images in case 3, acquired from signals at (a) transceiver A, (b) receiver B, (c) receiver C; (d) scan image of target model.

In case 3, the submarine moves with velocity vector $(0, -5, 3)$ m/s, in opposite direction to the SAS platform and towards the sea surface. Figs.11(a)-11(c) show the SAS images acquired with the signals received at transceiver A, receiver B and receiver C, respectively. Fig.11(d) shows the scan image viewed from transceiver A, which matches well in size and shape with the three SAS images. Compared with case 1, the additional heave motion in case 3 slightly orients the bow towards $-r$ direction in the images.

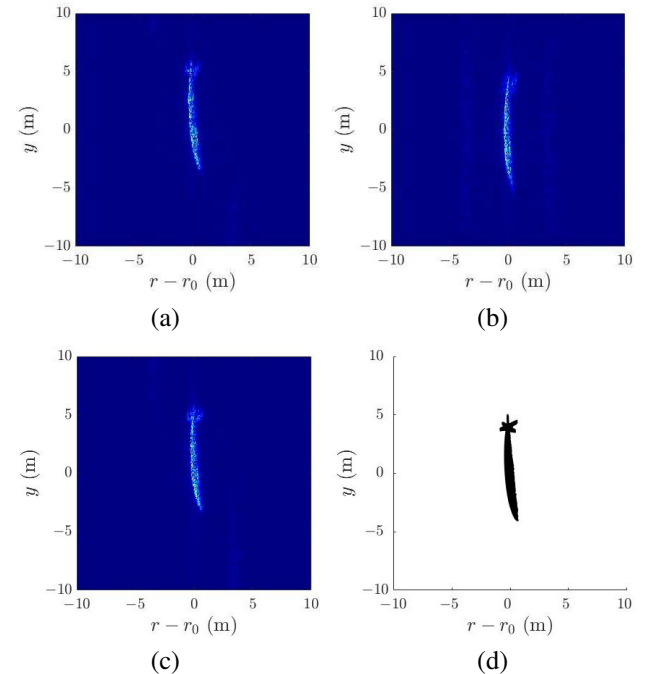


Fig. 12. SAS images in case 4, acquired from signals at (a) transceiver A, (b) receiver B, (c) receiver C; (d) scan image of target model.

Case 4 is designed to compare with case 3. The submarine moves with velocity vector $(0, -5, -3)$ m/s, in opposite direction to the SAS platform and towards the seabed. The three SAS images acquired with the scattered signals received at transceiver A, receiver B and receiver C, respectively, and the scan image in Fig.12(d) match well in size and shape.

In case 3, the submarine moves upwards and the bow is oriented towards $-r$ direction in the images. In case 4, the submarine moves downwards and the bow is oriented towards r direction. Note that the moving direction of submarine can be determined more reliably from its velocity vector estimated in Section V than barely from the bow orientation in the images.

In case 5, the submarine moves with velocity vector $(1.5, 8, 1)$ m/s, in the same direction and faster than the SAS platform, bearing some sway and heave motions. The SAS images in Figs.13(a) and 13(c) look blurred, while that in Fig.13(b) clearly reveals the target shape and size, possibly because the hull flank of the submarine is well exposed to receiver B than to transceiver A or receiver C.

In case 6, the submarine moves with velocity vector $(3, -5, 3)$ m/s, in an opposite direction to the SAS platform, swaying away from the latter and rising towards the sea surface. Case 6 is extended from case 3, and can also be compared with cases 4 and 5. The submarine in cases 3 and

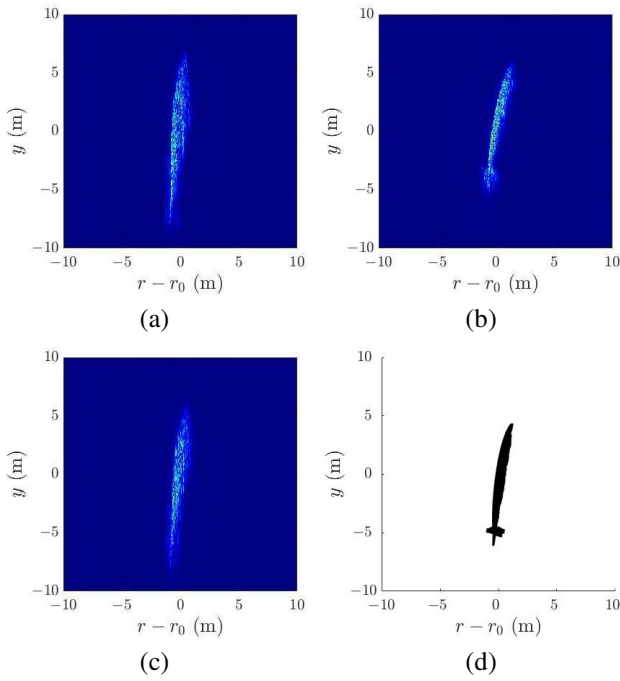


Fig. 13. SAS images in case 5, acquired from signals at (a) transceiver A , (b) receiver B , (c) receiver C ; (d) scan image of target model.

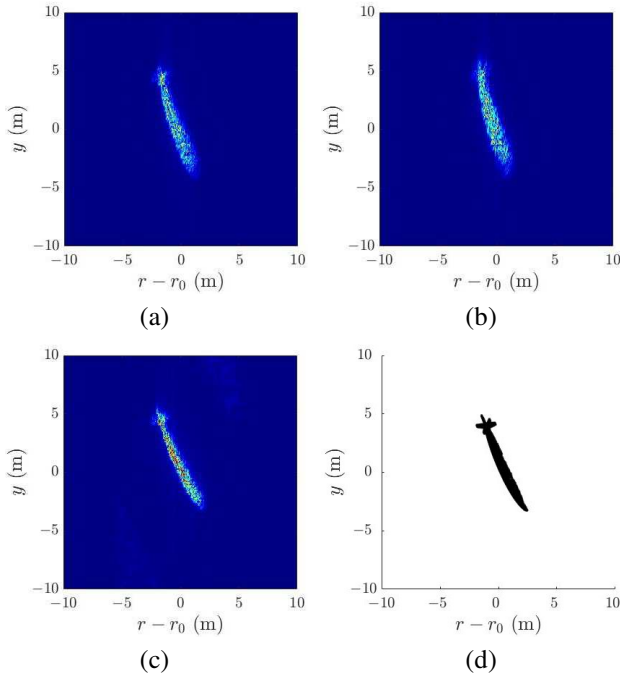


Fig. 14. SAS images in case 6, acquired from signals at (a) transceiver A , (b) receiver B , (c) receiver C ; (d) scan image of target model.

4 heaves in opposite direction. Its bow is oriented towards r direction in the images if the heave velocity is negative, and vice versa. With the additional sway motion in case 6, the bow is oriented towards r direction. Note that the r coordinate of a scatterer is mapped from its x and z coordinates, thus using the bow orientation to judge the heave motion is not definite.

The SAS images acquired with signals from transceiver A and receiver B in case 6 are more blurred than their

counterparts in case 5, while that acquired with signals from receiver C in case 6 is clearer than its counterpart in case 5, because a large chunk of hull flank is exposed to receiver C .

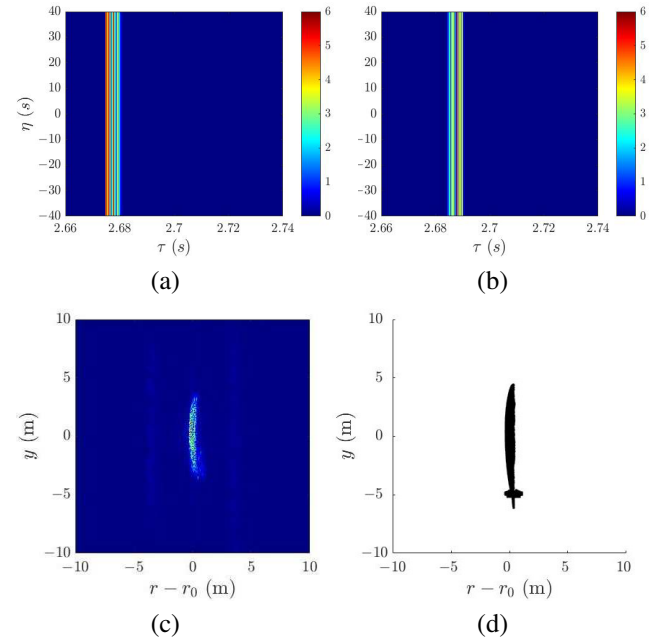


Fig. 15. SAS signals in case 7: (a) received baseband signal $s_{rb1}(\tau, \eta)$ at transceiver A , (b) received baseband signal $s_{rb2}(\tau, \eta)$ at receiver B , (c) SAS image acquired from signals at receiver C ; (d) scan image of target model.

In case 7, the submarine moves at exactly the same speed and direction as the SAS platform. Figs.15(a) and 15(b) show the magnitude of received baseband signals $s_{rb1}(\tau, \eta)$ at transceiver A and $s_{rb2}(\tau, \eta)$ at receiver B , respectively. Under this circumstance, the values of K'_{a1} in (5), K''_{a1} in (6) and K''_{a2} in (25) become zero, leading to $K_{a1,eq} = 0$ and $K_{a2,eq} = 0$. As a consequence, azimuth compression cannot be conducted with $H_{ac1}(f_\eta)$ in (19) and $H_{ac2}(f_\eta)$ in (31), hence image cannot be focused in the azimuth direction. From another perspective, the features in Figs.15(a) and 15(b) indicate the submarine moves at the same speed and direction as the SAS platform.

Fig.15(c) shows the SAS image acquired with the signals at receiver C . Since there is relative motion between the submarine and the stationary receiver C , a SAS image is acquired and matches well with the scan image in Fig.15(d), viewed from transceiver A . Note that the velocity vector can still be accurately estimated with the method in Section V.

In case 8, the submarine moves in x direction. Figs.16(a)-16(c) show the SAS images acquired with the signals at transceiver A , receiver B and receiver C , respectively. Fig.16(d) shows the scan image viewed from transceiver A . The starboard flank in Figs.16(a)-16(c) looks sharp, but the port flank spreads in y direction, the rudders and propeller at the stern are hardly recognizable, but the velocity vector can still be accurately estimated with the method in Section V. One may steer the SAS platform to align with the submarine moving direction to acquire at least one focused SAS image, as in the previous cases.

Fig.17 shows a schematic to explain the image blurring in

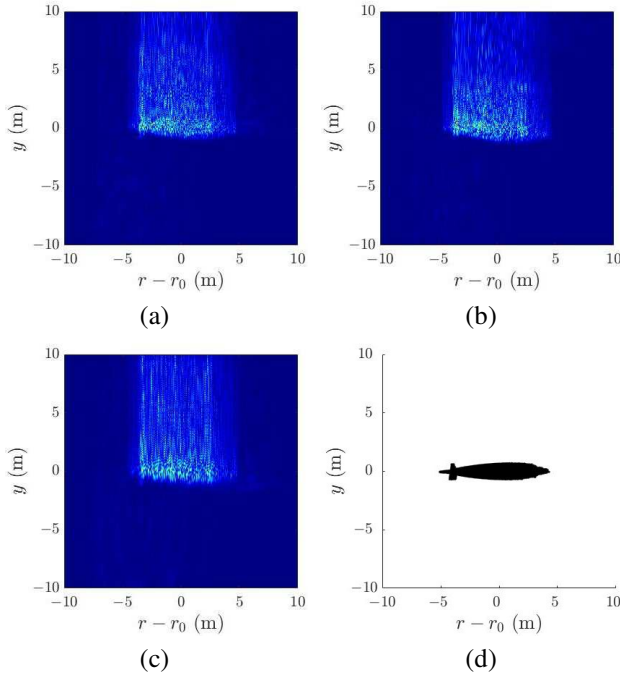


Fig. 16. SAS images in case 8, acquired from signals at (a) transceiver A, (b) receiver B, (c) receiver C; (d) scan image of target model.

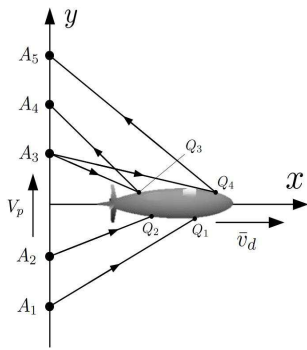


Fig. 17. Schematic to explain image blurring in case 8.

case 8. The SAS platform moves in y direction at speed V_p , and the submarine moves in x direction with velocity vector $\bar{v}_d = \hat{x}v_x$. When the SAS platform passes by A_1 , it emits an acoustic pulse to reach a scatterer Q_1 on the submarine, but some scattered wave maybe blocked by the hull from being received by any of the three receivers. Similarly, when the SAS platform passes by A_2 , it emits another acoustic pulse to reach a scatterer Q_2 on the submarine, and some scattered wave maybe blocked again by the hull. It appears that the acoustic pulses emitted by transceiver A at $y < 0$ are easily blocked by the hull from being received, and the bottom half ($y < 0$) of the SAS images displays little blurring.

On the other hand, when the SAS platform passes by A_3 (at η_3), it emits an acoustic pulse to reach scatterers Q_3 and Q_4 on the submarine, the difference of path-lengths between $A_3-Q_3-A_4$ and $A_3-Q_4-A_5$ is significant that the scattered signals reach A_4 (at $\eta = \eta_4$) and A_5 (at $\eta = \eta_5$) at different slow times, hence the upper part ($y > 0$) of SAS images becomes blurred due to mixture of delayed echoes from previous pulses.

In all these cases, the velocity vector of the target can always be estimated with error lower than 3 %, by using the proposed method in Section V. In most cases, at least one SAS image can be well focused to restore the shape and size of the moving target.

VII. FURTHER DISCUSSIONS

A. Verification with SOTA Methods

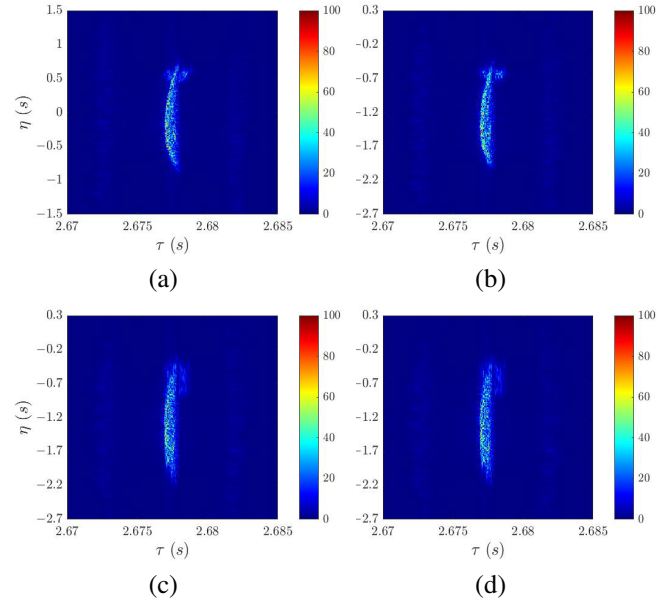


Fig. 18. SAS images in case 1, (a) proposed approach with estimated velocity vector $(0.002, -3.914, 0)$ m/s, (b) conventional RDA, (c) CSA, (d) omega-KA [39], (b)-(d) are acquired using the given velocity vector of $(0.002, -3.914, 0)$ m/s.

To verify the efficacy of the proposed method, three SOTA imaging algorithms referred to in Section I are implemented for comparison, including conventional range Doppler algorithm (RDA), chirp scaling algorithm (CSA), and omega-K algorithm (ω KA) [39]. The stop-and-go assumption is purposely imposed on these three algorithms to study its effects on SAS imaging.

Fig.18 shows the acquired SAS images in case 1, by using the proposed method and these three SOTAs [39], respectively. The four images reveal well-focused submarines, with their size, shape and range almost identical. However, Figs.18(b)-18(d) show that the acquired SAS images with the three SOTAs, under the stop-and-go assumption, are shifted by about 1s in the azimuth direction compared with that in Fig.18(a), manifesting the effects of stop-and-go assumption on the azimuth positioning.

Two images \bar{x} and \bar{y} can be compared in a quantitative way by using a structural similarity (SSIM) index [52]

$$\text{SSIM}(\bar{x}, \bar{y}) = L^\alpha(\bar{x}, \bar{y}) C^\beta(\bar{x}, \bar{y}) S^\gamma(\bar{x}, \bar{y})$$

where

$$L(\bar{x}, \bar{y}) = \frac{2\mu_x\mu_y + C_1}{\mu_x^2 + \mu_y^2 + C_1}$$

$$C(\bar{x}, \bar{y}) = \frac{2\sigma_x\sigma_y + C_2}{\sigma_x^2 + \sigma_y^2 + C_2}$$

$$S(\bar{x}, \bar{y}) = \frac{\sigma_{xy} + C_3}{\sigma_x\sigma_y + C_3}$$

are specified for comparing luminance, contrast and structure, respectively; μ_η and σ_η are the mean and standard deviation, respectively, of image $\bar{\eta}$, with $\eta = x, y$, and σ_{xy} is the covariance between \bar{x} and \bar{y} . The value of SSIM index lies in $[0, 1]$, and is equal to one if two images are identical.

The SSIM index is 0.9398 between Figs.18(a) and 18(b), 0.9111 between Figs.18(a) and 18(c), and 0.9082 between Figs.18(a) and 18(d). All three SSIM indices are above 0.9, indicating high similarities between these SAS images. Thus, the efficacy of the proposed method is verified.

B. Two Independent Targets

The proposed method can be extended to acquire images in more complicated situations. For example, consider a scenario with two submarines at same depth and separated by 50 meters. The first submarine moves with the velocity vector as in case 1, and the second submarine moves with the velocity vector as in case 3.

Fig.19(a) shows two streaks of received signals, each attributed to a moving submarine. Fig.19(b) shows the magnitude of $S_{\text{wv}}(f_p, f_\eta)$ defined in (13), where two significant peaks reveal two targets moving with different motion parameters. The strongest peak pointed by a white arrow leads to an estimated azimuth FM rate of $\tilde{K}_{a1,eq} = 4.713$ Hz/s, compared with the true value of $K_{a1,eq} = 4.860$ Hz/s. Fig.19(c) shows the Radon transform of $s_{\text{rcmc1}}(\tau, \eta)$ in (17). The peak pointed by a white arrow leads to an estimated Doppler centroid frequency of $\tilde{f}_{dc1,eq} = 6.321$ Hz. Fig.19(d) shows the SAS image acquired with the estimated motion parameters. The blurred slivers near the left border are attributed to the second target. Fig.19(e) shows the zoom-in image of the first submarine, which is well focused.

The received signals attributed to the second submarine are extracted by removing from the original received signals the contribution of the first submarine. The latter is obtained by applying a series of reverse processes, including inverse AC, inverse RWC and inverse RCMC, on the acquired image of the first submarine. Then, the extracted signals are processed to acquire the image of the second submarine. Fig.19(f) shows the magnitude of $S_{\text{wv}}(f_p, f_\eta)$ on the extracted signals, where the peak reveals the second moving target. The estimated azimuth FM rate is $\tilde{K}_{a1,eq} = 7.203$ Hz/s, compared with the true value of $K_{a1,eq} = 7.250$ Hz/s. Fig.19(g) shows the Radon transform of $s_{\text{rcmc1}}(\tau, \eta)$ on the second target. The peak leads to an estimated Doppler centroid frequency of $\tilde{f}_{dc1,eq} = -80.985$ Hz. Fig.19(h) shows the acquired SAS image of the second submarine, which is close to that in case 3. The proposed method can be iterated to acquire SAS images of multiple targets moving with different motion parameters.

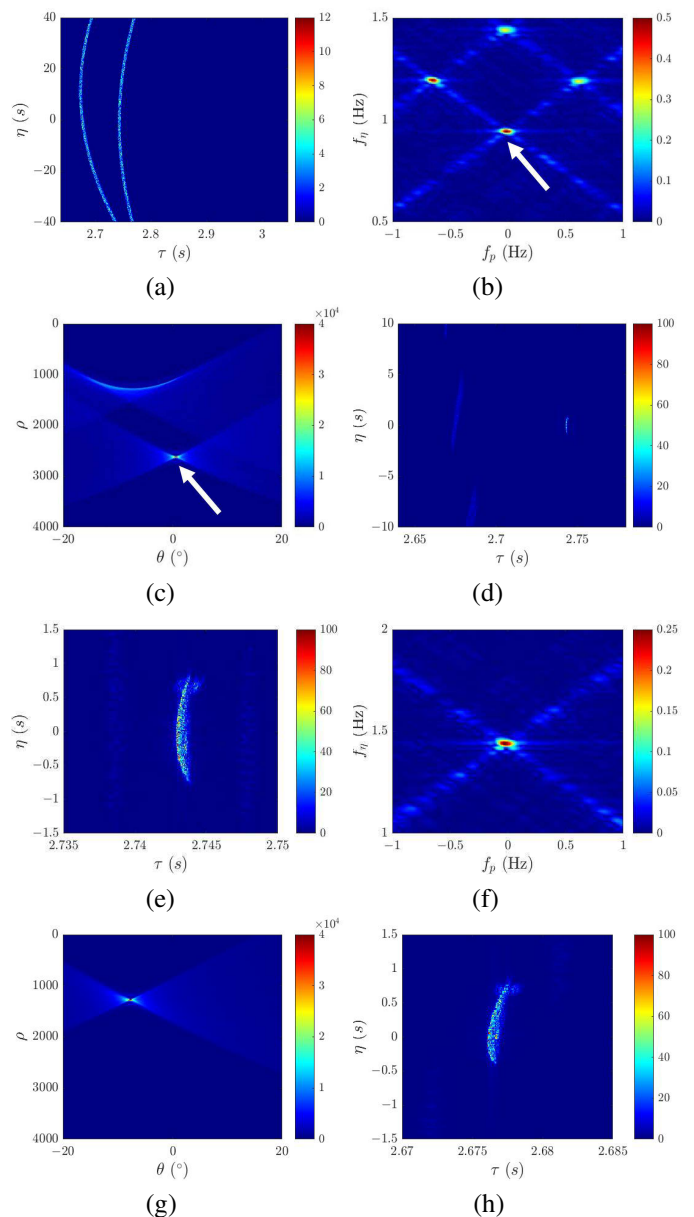


Fig. 19. Magnitude of (a) received signals from two moving targets, (b) $S_{\text{wv}}(f_p, f_\eta)$, (c) Radon $\{s_{\text{rcmc1}}(\tau, \eta)\}$ of first target, (d) $s_{18}(\tau, \eta)$ of first target, (e) $s_{18}(\tau, \eta)$ of first target (zoomed in), (f) $S_{\text{wv}}(f_p, f_\eta)$ of second target, (g) Radon $\{s_{\text{rcmc1}}(\tau, \eta)\}$ of second target, (h) $s_{18}(\tau, \eta)$ of second target.

C. Effects of Noise

In this Subsection, the proposed method is put to test under a noisy environment. Additive white Gaussian noise at given level is added to the received signal $s_{\text{rb1}}(\tau, \eta)$ in (7) to form $s_{\text{rb1,n}}(\tau, \eta)$, which is processed by the flow-chart in Fig.3 to obtain $s_{18,n}(\tau, \eta)$. It is observed that an discernible peak can be found on $S_{\text{wv}}(f_p, f_\eta)$ in (13) when SNR is above certain level. Once a peak is identified, the motion parameters can be estimated and a SAS image can be acquired. On the other hand, too much noise will bury the peak on $S_{\text{wv}}(f_p, f_\eta)$, disabling the subsequent SAS imaging process.

Figs.20(a) and 20(b) show the magnitude of noise-free received signal $s_{\text{rb1}}(\tau, \eta)$ and $s_{\text{rb1,n}}(\tau, \eta)$ with SNR = -15

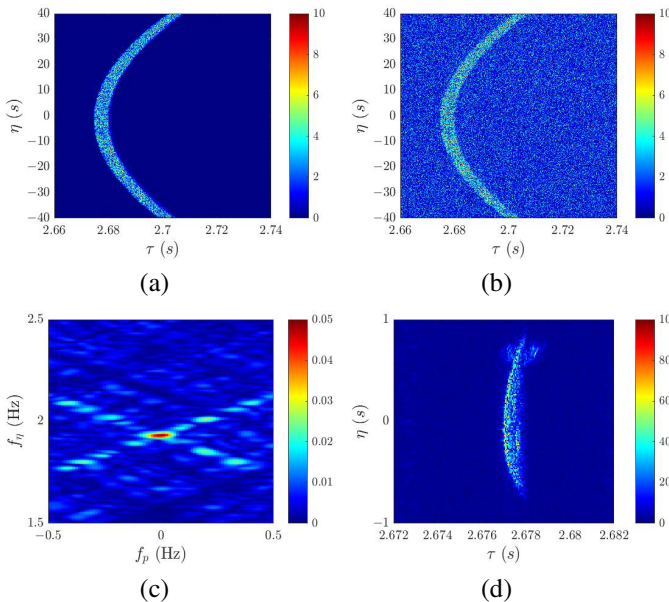


Fig. 20. Magnitude of (a) $s_{rb1}(\tau, \eta)$ at transceiver A in case 1, (b) $s_{rb1,n}(\tau, \eta)$, SNR = -15 dB, (c) $S_{wv}(f_p, f_\eta)$, (d) $s_{18,n}(\tau, \eta)$.

dB, respectively, at transceiver A in case 1. Fig.20(c) shows the magnitude of $S_{wv}(f_p, f_\eta)$ on $s_{rb1,n}(\tau, \eta)$. An obvious peak can be identified, thus $\tilde{K}_{a1,eq}$ and $\tilde{f}_{dc1,eq}$ can be estimated. Fig.20(d) shows the acquired SAS image, which is well focused. Similar approach is applied to received signals at receivers B and C. The Doppler centroids are estimated as $\tilde{f}_{dc1,eq} = 6.331$ Hz, $\tilde{f}_{dc2,eq} = -79.592$ Hz, $\tilde{f}_{dc3,eq} = 2.605$ Hz, respectively. Thus, the velocity vector is estimated as $(\tilde{v}_x, \tilde{v}_y, \tilde{v}_z) = (0.006, -3.922, 0.001)$ m/s, with an error is 1.956 %.

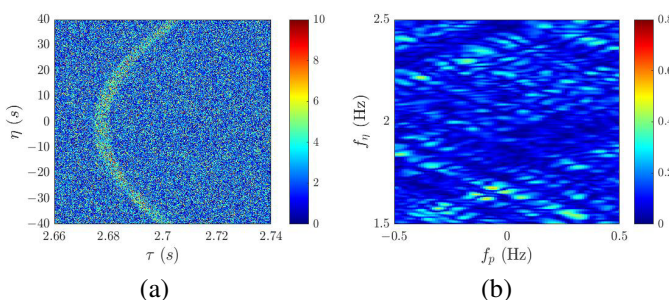


Fig. 21. Magnitude of (a) $s_{rb1,n}(\tau, \eta)$ at transceiver A in case 1, SNR = -20 dB. (b) $S_{wv}(f_p, f_\eta)$.

Fig.21(a) shows the magnitude of received signal $s_{rb1,n}(\tau, \eta)$, with SNR = -20 dB. Fig.21(b) shows the magnitude of $S_{wv}(f_p, f_\eta)$, on which no peak can be identified with confidence, which implies the parameter $\tilde{K}_{a1,eq}$ cannot be estimated, hence the SAS imaging process is halted.

Fig.22 shows the percentage error of velocity vector lies between 1.8% and 2.2% with $\text{SNR} \geq -17$ dB. Beyond that, the peak position on $S_{wv}(f_p, f_\eta)$ cannot be determined, hence the proposed method no longer applies.

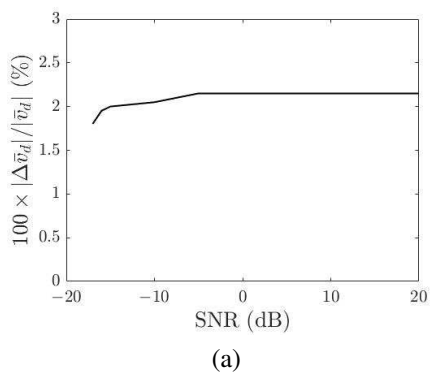


Fig. 22. Percentage error of velocity vector versus SNR.

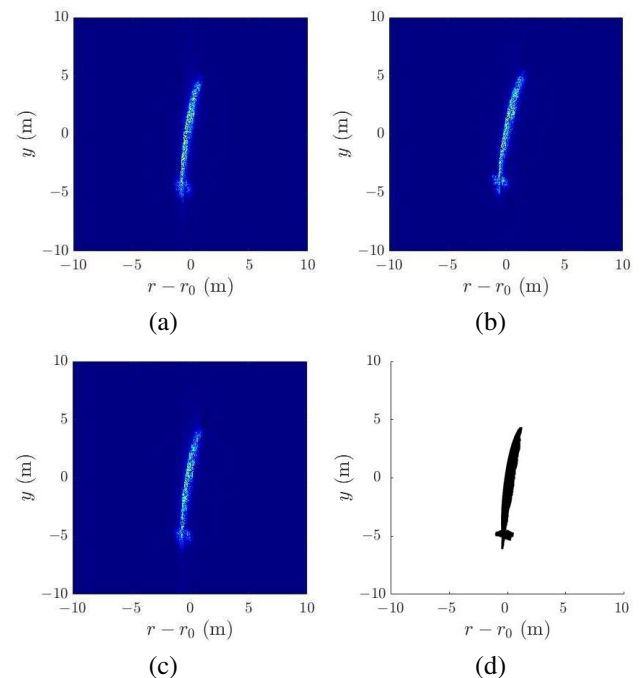


Fig. 23. SAS images in case 5, autofocus with PGA, acquired from signals at (a) transceiver A, (b) receiver B, (c) receiver C; (d) scan image of target model.

D. Image Autofocus

As shown in Section VI, the SAS images in cases 5, 6 and 8 are blurred, possibly related to the sway motion of the target. Image autofocus methods such as phase gradient autofocus (PGA) [53], [54] will be tried to focus the blurred images. The PGA is a non-parametric method commonly used to compensate unpredictable phase perturbations embedded in the received signal or induced during the imaging process. The gradient of the unwanted phase error is computed directly from the blurred SAS image, which is then used to compensate the phase error.

Figs.23(a)-23(c) show the PGA-autofocused SAS images from their counterparts in Figs.13(a)-13(c), respectively; Figs.24-24(c) show the PGA-autofocused SAS images from their counterparts in Figs.14(a)-14(c), respectively; and Figs.25(a)-25(c) show the PGA-autofocused SAS images from their counterparts in Figs.16(a)-16(c), respectively. The PGA

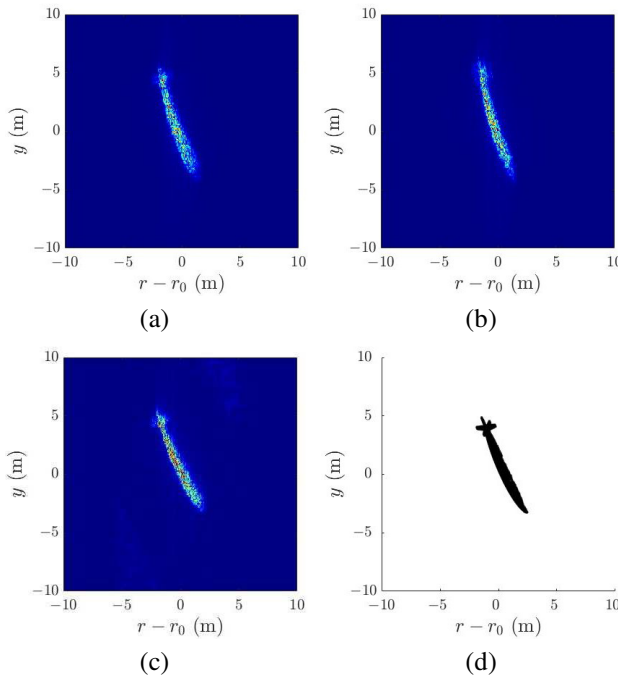


Fig. 24. SAS images in case 6, autofocus with PGA, acquired from signals at (a) transceiver A, (b) receiver B, (c) receiver C; (d) scan image of target model.

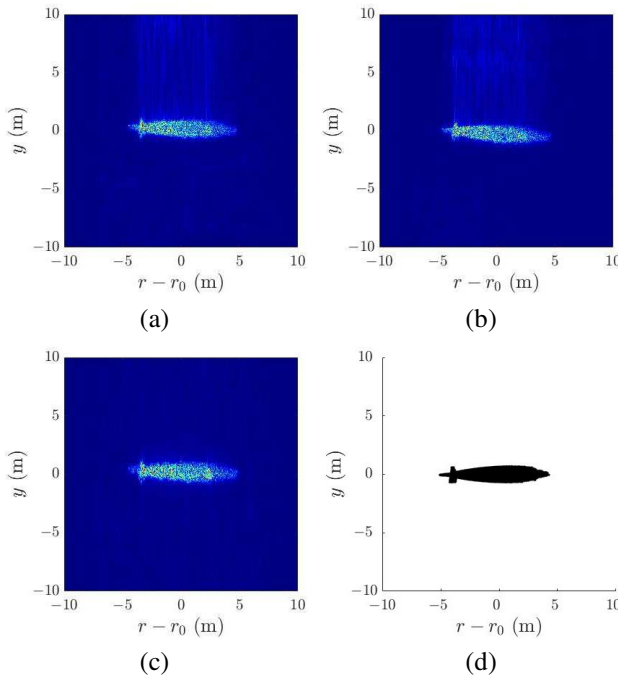


Fig. 25. SAS images in case 8, autofocus with PGA, acquired from signals at (a) transceiver A, (b) receiver B, (c) receiver C; (d) scan image of target model.

works marvelously well on case 8, in which the smudge due to sway motion is the strongest among the three cases.

E. Computational Load

The computational load of the proposed approach is the sum of computational loads required in all the algorithms

delineated in the flow-chart of Fig.3. Table III lists the computational load of algorithms constituting the proposed approach, where N_r and N_a are the number of range bins and azimuth bins, respectively, FT, IFT and FFT are the abbreviations of Fourier transform, inverse Fourier transform and fast Fourier transform, respectively.

TABLE III
COMPUTATIONAL LOAD OF CONSTITUENT ALGORITHMS.

algorithm	computational load	ref.
range FT (2D FFT)	$O(N_r N_a \log_2(N_r N_a))$	[39]
range compression	$O(N_r N_a)$	[39]
RFRT	$O(N_r N_a)$	[40]
SoWVD	$O(2N_a^2 \log_2 N_a)$	[27]
RCMC	$O(N_r N_a)$	
Radon transform	$O(N_r N_a \log_2(N_r N_a))$	[55]
RW compensation	$O(N_r N_a)$	
azimuth FT (2D FFT)	$O(N_r N_a \log_2(N_r N_a))$	[39]
range IFT	$O(N_r N_a \log_2(N_r N_a))$	
azimuth compression	$O(N_r N_a)$	[39]
azimuth IFT	$O(N_r N_a \log_2(N_r N_a))$	

F. Comparison with Other Viable Sonar Techniques

Many methods have been proposed to track multiple underwater moving targets with the use of acoustic vision in recent decades. A forward-looking sonar (FLS) is capable of positioning an underwater moving target, which is crucial for the deployment of autonomous underwater vehicles (AUVs) [56]. The key features of a moving target in sonar imaging may vary significantly when its relative motion with the AUV changes. The intensity and shape of the same target may appear quite different if the moving direction, orientation or relative distance is altered. Nonlinear motion of a target makes its tracking more difficult, because many more motion parameters need to be estimated.

In [56], an FLS imaging and tracking method based on Gaussian particle filter (GPF) were proposed to track multiple targets in a cluttered underwater environment. A generalized regression neural network (GRNN) was used to extract key features of targets to sort them into different classes, followed by multi-feature adaptive fusion to establish adequate GPF for target tracking in complex environment. The proposed method was verified by conducting field experiment in a tank and an offshore environment, respectively. The results suggest that multiple simple targets can be tracked at the same time, with their courses estimated from received sonar echoes at fixed intervals.

Similar situations have been presented and discussed in Section VI of our work, where 8 cases are designed with different linear motions and orientations of moving target. The acquired image in each case reveals different flanks of the moving target from different view angles. The simulation results suggest that SAS imaging on a specific flank of submarine can be obtained by adjusting proper relative motion between the SAS platform and the moving target. In short, [56] focuses on the tracking of target moving routes with the use of sonar. Our work focuses on the imaging of moving target under linear motion.

In Sections III and IV of our work, the target is assumed to move at constant speed in a given direction. To account for the acceleration due to target maneuvering, a more complicated range model is required, and more motion parameters need to be estimated from the received signals with more sophisticated algorithms. We will develop relevant models and present the results in the future work.

Mechanically scanned imaging sonar (MSIS), commonly used for seabed prospecting and underwater navigation, is capable of producing high-resolution images over a narrow spatial range [57]. MSIS is usually deployed at a fixed position, restricting its capability to estimate the position of an object. Underwater target tracking with acoustic methods plays a crucial role in the navigation of underwater autonomous vehicles, which requires to update the vehicle position and attitude periodically. A practical alternative is to prepare a database of synthetic sonar images by using the precise bathymetric data over the area of interest. A comparative navigation approach is then used to determine the target position in an MSIS image by searching for the best match between the MSIS image and the synthetic images in the database, aided with proper similarity functions or probability distributions.

In our work, transceiver *A* and receiver *B* move with the platform, while receiver *C* is attached to a stationary sonobuoy. The echoed signals from a moving target will display relative motion in at least one of the receivers, which holds the premise for SAS imaging technique to work properly. The stationary sonobuoy plays a similar role as an MSIS deployed at fixed position.

In [58], a noise-driven optimization method was proposed for an active target tracking FLS system, where the noise was modeled as white additive noise under most circumstances. In our work, the target position and shape are revealed in the acquired SAS image. The target speed is estimated with the Doppler centroid frequencies derived from the scattered signals at three different receivers. The noise has negative impact on our method. The simulation results verify that with $\text{SNR} > -17 \text{ dB}$, the SAS image can be well-focused and the velocity vector can be accurately estimated and is insensitive to the noise level.

G. Simulations versus Field Measurements

Simulations have been widely used to study different phenomena and parameters of interest. Simulation scenarios can be designed with more flexibility and exempted from environmental interference or noise. Moreover, simulation can be done in scenarios which are difficult if not impossible to conduct in field measurements. Field experiments are usually persuasive to validate a proposed method, but field measurements in the ocean are expensive, requiring special skills to operate relevant apparatuses and proper conditions like weather to collect valid data. Alternative measurement in a hydraulics laboratory requires the removal of echoes from surrounding environments, which is no easy task. Even when measurement data are available, simulations can also be used to diagnose the data for possible flaws in instruments or procedures.

An alternative to verify the proposed method is to compare with the simulation results of compatible SOTA methods. To

demonstrate the efficacy of the proposed method in practical applications, the simulation scenarios and parameters are carefully selected to fit the real-world situations as much as possible. Experts in field measurements may use our model to facilitate their measurement procedure as well.

H. Highlights of Contributions

The novelty and technical contributions of this work are summarized as follows.

- (1) This is the first article providing a complete procedure on multistatic SAS imaging of moving submarines.
- (2) Rigorous formulations on the imaging of moving submarines are presented, under non-stop-and-go premise. Most SAS models in the literature were developed for imaging of stationary targets like seabed, and the formulations were usually incomplete.
- (3) The RFRT is used to concentrate the signals into lines around $\tau = 0$, the modified SoWVD transform is then applied to the concentrated signals to estimate the azimuth FM rate. The proposed method works well for SAS imaging, which is usually accompanied with significant range curvature. This work is the first one to integrate RFRT, Radon transform and modified SoWVD to acquire a focused SAS image of an underwater moving target.
- (4) This work is the first one to propose a multistatic configuration for SAS imaging, as well as a rigorous method for estimate the velocity vector of a underwater moving target, without prior knowledge.
- (5) In this work, we explore the possibility of integrating a sonobuoy for SAS imaging and velocity estimation on a moving target, increasing the flexibility and versatility for underwater SAS imaging, which has never been discussed in the literature before.
- (6) The simulation indicates that an SAS may malfunction if a target is moving with the same velocity as the SAS platform, which has never been discussed in the literature. To deal with such situation, we propose a feasible solution by deploying a stationary sonobuoy, against which a moving target must manifest relative motion. Thus, SAS imaging is guaranteed to work in the proposed multistatic SAS configuration.
- (7) This is the first work that elaborates the relative velocity can significantly affect the target size in the acquired image. Rigorous theory is provided and verified by simulating 8 scenarios, with the target moving with different velocity vectors.
- (8) This is the first work to propose the use of scan image projected from 3D target models to help verifying an acquired SAS image of a moving target and identifying it.
- (9) The proposed approach can acquire SAS images of a moving target and estimate its velocity vector in real time, without any prior knowledge. Hence, it can be used in real-time monitoring and surveillance of underwater vehicles, with the estimated velocity to predict their possible movements.

VIII. CONCLUSIONS

A multistatic SAS imaging configuration, composed of a transceiver, a towed receiver and a stationary sonobuoy, has been developed to acquire images of underwater moving targets. In the range model, the time delay between transmitted and received signals is accounted for, the chirp rate is estimated with RFRT and the modified SoWVD, and the Doppler centroid is estimated with Radon transform. A semi-analytical method is proposed to estimate the velocity vector of the moving target. Eight designate cases, with target moving in different directions and different speeds, are simulated to demonstrate the merits and limits of the proposed method. The velocity vector of the moving target can be estimated within 3% of error if the signal-to-noise ratio is higher than -17 dB. The SAS images mapped to the range-azimuth plane bear decent resemblance to the scan image projected from the 3D target model. The proposed approach has been verified with the results using conventional RDA, CSA and ω KA, respectively. Clear and recognizable SAS images and accurate velocity vector can be acquired if $\text{SNR} > -17$ dB. Images on multiple moving targets can be acquired iteratively. Blurred images can be enhanced with autofocus algorithms like PGA. Comparison with other viable sonar techniques and field measurements has also been briefly commented.

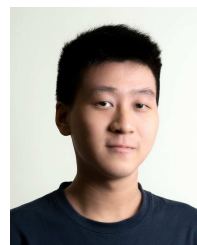
ACKNOWLEDGMENTS

The authors are grateful to the Reviewers, the Editor and the Associate Editor for their inspiring comments.

REFERENCES

- [1] G. G. Wren and D. May, "Detection of submerged vessels using remote sensing techniques," *Australian Defense Force J.*, no. 127, pp. 9-15, Nov./Dec. 1997.
- [2] T. Stefanick, "The nonacoustic detection of submarines," *Scientific American*, vol. 258, pp. 41-47, Mar. 1998.
- [3] Y. Chen and J. Yuan, "Methods of differential submarine detection based on magnetic anomaly and technology of probes arrangement," *Int. Workshop Materials Eng. Computer Sci.*, pp. 442-445, 2015.
- [4] S. Zhou and P. Willett, "Submarine location estimation via a network of detection-only sensors," *IEEE Trans. Signal Processing*, vol. 55, pp. 3104-3115, May 2007.
- [5] L. R. Warren, "Hull-mounted sonar/ship design evolution and transition to low-frequency applications," *IEEE J. Oceanic Eng.*, vol. 13, pp. 296-298, Oct. 1988.
- [6] V. Myers, I. Quidu, B. Zerr, T. O. Sæbø, and R. E. Hansen, "Synthetic aperture sonar track registration with motion compensation for coherent change detection," *IEEE J. Oceanic Eng.*, vol. 45, pp. 1045-1062, May 2019.
- [7] A. D'Amico and R. Pittenger, "A brief history of active sonar," *Aquatic Mammals*, vol. 35, pp. 426-434, Sep. 2010.
- [8] Y. Chen, C. Ni, and X. Wang, "Operational research for helicopter with dipping sonar to search submarine," *Int. Conf. Info. Sci. Control Eng.*, pp. 852-856, 2015.
- [9] R. B. Yoash, M. P. Atkinson, and M. Kress, "Where to dip? Search pattern for an antisubmarine helicopter using a dipping sensor," *Military Operation Res.*, vol. 23, pp. 19-40, 2018.
- [10] R. Song, H. Esmaiel, H. Sun, J. Qi, H. Zhang, and M. Zhou, "Multi-submarines detection using multistatic sonar system," *IEEE Info. Technol. Mechatronics Engineering Conf.*, pp. 1671-1675, Jun. 2020.
- [11] M. P. Hayes and P. T. Gough, "Synthetic aperture sonar: A review of current status," *IEEE J. Oceanic Eng.*, vol. 34, pp. 207-224, Jul. 2009.
- [12] D. J. Battle, P. Gerstoft, W. A. Kuperman, W. S. Hodgkiss, and M. Siderius, "Geoaoustic inversion of tow-ship noise via near-field-matched-field processing," *IEEE J. Oceanic Eng.*, vol. 28, pp. 464-467, Oct. 2003.
- [13] X. Zhang, J. Tang, and H. Zhong, "Multireceiver correction for the chirp scaling algorithm in synthetic aperture sonar," *IEEE J. Oceanic Eng.*, vol. 39, pp. 472-481, Jul. 2014.
- [14] D. A. Cook and D. C. Brown, "Analysis of phase error effects on stripmap SAS," *IEEE J. Oceanic Eng.*, vol. 34, pp. 250-261, Dec. 2008.
- [15] S. G. Kargl, K. L. Williams, and E. I. Thorsos, "Synthetic aperture sonar imaging of simple finite targets," *IEEE J. Oceanic Eng.*, vol. 37, pp. 516-532, Jul. 2012.
- [16] D. P. Williams, "Fast target detection in synthetic aperture sonar imagery: A new algorithm and large-scale performance analysis," *IEEE J. Oceanic Eng.*, vol. 40, pp. 71-92, Jan. 2015.
- [17] C. Noviello, G. Fornaro, and M. Martorella, "Focused SAR image formation of moving target based on Doppler parameter estimation," *IEEE Trans. Geosci. Remote Sensing*, vol. 53, pp. 3460-3470, Jun. 2015.
- [18] V. T. Vu, T. K. Sjogren, M. I. Pettersson, A. Gustavsson, and L. M. H. Ulander, "Detection of moving targets by focusing in UWB SAR - Theory and experimental results," *IEEE Trans. Geosci. Remote Sensing*, vol. 48, pp. 3799-3815, Oct. 2010.
- [19] P. Huang, G. Liao, Z. Yang, X.-G. Xia, J. Ma, and X. Zhang, "An approach for refocusing of ground moving target without target motion parameter estimation," *IEEE Trans. Geosci. Remote Sensing*, vol. 55, pp. 336-350, Sep. 2016.
- [20] T. Dang and Y. Xiang, "A fast two-dimensional velocity estimation method for multi-channel UWB SAR," *IEEE Access*, vol. 9, pp. 11427-11436, Jan. 2021.
- [21] Z. Li, J. Wu, Y. Huang, Z. Sun, and J. Yang, "Ground-moving target imaging and velocity estimation based on mismatched compression for bistatic forward-looking SAR," *IEEE Trans. Geosci. Remote Sensing*, vol. 54, pp. 3277-3291, Jun. 2016.
- [22] J. Yang, C. Liu, and Y. Wang, "Imaging and parameter estimation of fast-moving targets with single-antenna SAR," *IEEE Geosci. Remote Sensing Lett.*, vol. 11, pp. 529-533, Jul. 2013.
- [23] W. Wu, G. H. Wang, and J. P. Sun, "Polynomial Radon-polynomial Fourier transform for near space hypersonic maneuvering target detection," *IEEE Trans. Aerospace Electronic Syst.*, vol. 54, pp. 1306-1322, Dec. 2017.
- [24] W. Wu, G. Wang, and J. Sun, "A variable-diameter-arc-helix Radon transform for detecting a near space hypersonic maneuvering target," *IEEE Access*, vol. 7, pp. 184875-184884, Dec. 2019.
- [25] S. Barbarossa, "Analysis of multicomponent LFM signals by a combined Wigner-Hough transform," *IEEE Trans. Signal Processing*, vol. 43, pp. 1511-1515, Jun. 1995.
- [26] J. C. Wood and D. T. Barry, "Radon transformation of time-frequency distributions for analysis of multicomponent signals," *IEEE Trans. Signal Processing*, vol. 42, pp. 3166-3177, Nov. 1994.
- [27] P. Huang, G. Liao, Z. Yang, X.-G. Xia, J.-T. Ma, and X. Zhang, "A fast SAR imaging method for ground moving target using a second-order WVD transform," *IEEE Trans. Geosci. Remote Sensing*, vol. 54, pp. 1940-1956, Nov. 2015.
- [28] G. Wang and X.-G. Xia, "Synthetic aperture sonar imaging using joint time-frequency analysis," *Proc. SPIE*, vol. 3723, Mar. 1999.
- [29] S. Sun, Y. Chen, L. Qiu, G. Zhang and C. Zhao, "Inverse synthetic aperture sonar imaging of underwater vehicles utilizing 3-D rotations," *IEEE J. Oceanic Eng.*, vol. 45, pp. 563-576, Apr. 2020.
- [30] J. Chatillon, M. E. Bouhier and M. E. Zakharie, "Synthetic aperture sonar for seabed imaging: Relative merits of narrow-band and wide-band approached," *IEEE J. Oceanic Eng.*, vol. 17, pp. 95-105, Jan. 1992.
- [31] R. E. Hansen, H. J. Callow, T. O. Sæbø and S. A. V. Synnes, "Challenges in seafloor imaging and mapping with synthetic aperture sonar," *IEEE Trans. Geosci. Remote Sensing*, vol. 49, pp. 3677-3687, Oct. 2011.
- [32] J. Wang, J. Tang, and Z. Tian, " ω k algorithm for multi-receiver synthetic aperture sonar based on exact analytical two-dimensional spectrum," *J. Engineering*, vol. 2019, pp. 7210-7214, Oct. 2019.
- [33] X. Zhang, C. Tan, and W. Ying, "An imaging algorithm for multireceiver synthetic aperture sonar," *Remote Sensing*, vol. 11, p. 672, Mar. 2019.
- [34] R. E. Hansen, A. P. Lyons, T. O. Sæbø, H. J. Callow and D. A. Cook, "The effect of internal wave-related features on synthetic aperture sonar," *IEEE J. Oceanic Eng.*, vol. 40, pp. 621-631, Jul. 2015.
- [35] A. Bellettini and M. Pinto, "Design and experimental results of a 300-kHz synthetic aperture sonar optimized for shallow-water operations," *IEEE J. Oceanic Eng.*, vol. 34, pp. 285-293, Jul. 2009.
- [36] J. E. Piper, K. W. Commander, E. I. Thorsos and K. L. Williams, "Detection of buried targets using a synthetic aperture sonar," *IEEE J. Oceanic Eng.*, vol. 27, pp. 495-504, Jul. 2002.
- [37] D. P. Williams, "Underwater target classification in synthetic aperture sonar imagery using deep convolutional neural networks," *Int. Conf. Pattern Recognition*, 2016.

- [38] P. T. Gough and D. W. Hawkins, "Imaging algorithms for a strip-map synthetic aperture sonar: Minimizing the effects of aperture errors and aperture undersampling," *IEEE J. Oceanic Eng.*, vol. 22, pp. 27-39, Jan. 1997.
- [39] I. G. Cumming and F. H. Wong, *Digital Processing of Synthetic Aperture Radar Data: Algorithms and Implementation*, Norwood, MA: Artech House, 2005.
- [40] P. Huang, X.-G. Xia, Y. Gao, X. Liu, G. Liao, and X. Jiang, "Ground moving target refocusing in SAR imagery based on RFRT-FrFT," *IEEE Trans. Geosci. Remote Sensing*, vol. 57, pp. 5476-5492, Apr. 2019.
- [41] L. J. Cutrona, "Additional characteristics of synthetic aperture sonar systems and a further comparison with nonsynthetic aperture sonar systems," *J. Acous. Soc. Am.*, 61(5), pp. 1213-1217, 1977.
- [42] F. Jean, "Shadows, a new synthetic aperture sonar system, by IXSEA SAS," *OCEANS, Asia Pacific*, May 2006.
- [43] R. E. Hansen, T. O. Sæbø, H. J. Callow, and P. E. Hagen, "The SENSOOTEK synthetic aperture sonar-Results from HUGIN AUV trials," Norwegian Defense Research Establishment (FFI), Kjeller, Norway, Rep. 2007/01597, Jun. 2007.
- [44] A. Caiti, S. M. Jesus, and A. Kristensen, "Geoacoustic seafloor exploration with a towed array in a shallow water area of the Strait of Sicily," *IEEE J. Oceanic Eng.*, vol. 21, pp. 355-366, Oct. 1996.
- [45] C. Park, W. Seong, and P. Gerstoft, "Geoacoustic inversion in time domain using ship of opportunity noise recorded on a horizontal towed array," *J. Acous. Soc. Am.*, vol. 117, pp. 1933-1941, Apr. 2005.
- [46] M. A. Pinto *et al.*, "Experimental investigations into high resolution sonar systems," *MTS/IEEE Oceans*, vol. 2, pp. 916-922, Sep. 1999.
- [47] D. Marx, M. Nelson, E. Chang, W. Gillespie, A. Putney, and K. Warman, "An introduction to synthetic aperture sonar," *IEEE Workshop Statistical Signal Array Processing*, pp. 717-721, Aug. 2000.
- [48] A. Putney, E. Chang, R. Chatham, D. Marx, M. Nelson, and L. K. Warman, "Synthetic aperture sonar- The modern method of underwater remote sensing," *IEEE Aerospace Conf.*, vol. 4, pp. 4/1749-4/1756, Mar. 2001.
- [49] N. Friedman and J. L. Christley, *U.S. Submarines since 1945: An Illustrated Design History*, Annapolis, MD: Naval Institute Press, 1994.
- [50] P. Bachant, "USS Albacore submarine," *grabcad.com*, Jun. 28, 2015. [Online] <http://grabcad.com/library/uss-albacore-submarine-1>. [Accessed Sep. 4, 2021].
- [51] P. Cignoni, M. Callieri, M. Corsini, M. Dellepiane, F. Ganovelli, and G. Ranzuglia, "MeshLab: An open-Source mesh processing tool," *Eurographics Italian Chapter Conf.*, pp. 129-136, 2008.
- [52] Z. Wang, A. C. Bovik, H. R. Sheikh and E. P. Simoncelli, "Image quality assessment: From error visibility to structural similarity," *IEEE Trans. Image Processing*, vol. 13, pp. 600-612, Apr. 2004.
- [53] H. J. Callow, M. P. Hayes and P. T. Gough, "Stripmap phase gradient autofocus," *Oceans*, pp. 2414-2421, vol. 5, 2003.
- [54] D. E. Wahl, P. H. Eichel, D. C. Ghiglia and C. V. Jakowitz, "Phase gradient autofocus- A robust tool for high resolution SAR phase correction," *IEEE Trans. Aero. Electron. Syst.*, vol. 30, no. 3, pp. 827-835, July 1994.
- [55] W. A. Götz and H. J. Druckmüller, "A fast digital radon transform- An efficient means for evaluating the Hough transform," *Pattern Recognition*, vol. 29, pp. 711-178, Apr. 1996.
- [56] T. Zhang, S. Liu, X. He, H. Huang and K. Hao, "Underwater target tracking using forward-looking sonar for autonomous underwater vehicles," *Sensors*, vol. 20, p. 102, Dec. 2019.
- [57] N. Wawrzyniak and A. Stateczny, "MSIS image positioning in port areas with the aid of comparative navigation methods," *Polish Maritime Res.*, vol. 24, pp. 32-41, 2017.
- [58] W. Kazimierski and G. Zaniewicz, "Determination of process noise for underwater target tracking with forward looking sonar," *Remote Sensing*, vol. 13, p. 1014, Mar. 2021.



Chou-Wei Kiang was born in Taipei, Taiwan, in 1999. He received his B.S. degree in electrical engineering from National Taiwan University, Taipei, Taiwan, in 2022. He is currently a research assistant in the Group of Electromagnetic Applications, National Taiwan University. His research interests include electromagnetic simulations and applications, optics, quantum physics and engineering, applied physics, signal processing, remote sensing, radar and sonar imaging and communication systems.



Jean-Fu Kiang received his Ph.D. degree in electrical engineering from the Massachusetts Institute of Technology, Cambridge, MA, USA, in 1989. Since 1999, he has been a Professor with the Department of Electrical Engineering and Graduate Institute of Communication Engineering, National Taiwan University. His research interest is to explore different ideas, theories and methods on various electromagnetic phenomena and possible applications, including remote sensing, radar signal processing, antennas, phased arrays, propagation, scattering, communications, and so on. Some of his works can be viewed in his website: http://cc.ee.ntu.edu.tw/~jfkiang/selected_publications.html.